

Feasibility of Using Dynamically Oscillating Surfaces to Control Tollmien-Schlichting Waves

by

Haley Dell'Orso

A Thesis Submitted to the Graduate

Faculty of Rensselaer Polytechnic Institute

in Partial Fulfillment of the

Requirements for the degree of

MASTER OF SCIENCE

Major Subject: **MECHANICAL ENGINEERING**

Approved by the
Examining Committee:

Michael Amitay, Thesis Adviser

Onkar Sahni, Committee Member

Jason Hicken, Committee Member

Rensselaer Polytechnic Institute
Troy, New York

July 2016
(For Graduation August 2016)

TABLE OF CONTENTS

LIST OF FIGURES	iii
ACKNOWLEDGMENTS	v
ABSTRACT	vi
1. INTRODUCTION	1
2. ACTUATOR DESIGN AND QUANTIFICATION	9
2.1 EAP Actuator Quantification and Testing	9
2.2 PDOS Actuator Design and Quantification	12
3. EXPERIMENTAL SETUP AND TECHNIQUES	19
4. RESULTS	24
5. CONCLUSIONS	39
REFERENCES	42

LIST OF FIGURES

Figure 1. Schematic of an EAP actuator.....	9
Figure 2. EAP actuator (a) before and (b) after an external voltage difference is applied.	10
Figure 3. EAP dimple peak-to-peak deflection for frequencies from 1 Hz to 500 Hz.	11
Figure 4. EAP dimple (a) DC offset and (b) maximum deflection for frequencies 1 Hz to 500 Hz.....	12
Figure 5. Exploded view of PDOS actuator used for optical table quantification.	13
Figure 6. Piezoelectric disk used in the PDOS actuator.	14
Figure 7. Setup of laser displacement sensors and PDOS actuator for optical table quantification.	15
Figure 8. Peak-to-peak rubber deflection for 0.79 mm and 0.39 mm thick rubber surfaces with circular dimples of 12.7 mm and 6.35 mm diameter, and for slot with dimensions 6.35 x 2 mm.	16
Figure 9. Peak-to-peak rubber deflection for neck heights ranging from 2 to 4 mm.	17
Figure 10. Rubber deflection for the PDOS actuator used in wind tunnel testing.	18
Figure 11. Picture of the flat plate wind tunnel setup looking from the (a) leading edge and (b) trailing edge.....	20
Figure 12. Experimental setup used for wind tunnel testing	21
Figure 13. Boundary layer profiles of the experimental data, the Blasius solution, and simulation results (obtained by Joe Eilert).	24
Figure 14. Phase-averaged streamwise velocity fluctuations observed at $x/L = 0.18$ and with upstream PDOS activated at $y_{PDOS}/\delta =$ (a) 0.9%, (b) 3.9%, and (c) 8.7%, and wall- normal velocity fluctuations observed at $x/L = 0.28$ with $y_{PDOS}/\delta =$ (d) 0.9%, (e) 3.9%, and (f) 8.7%.	26
Figure 15. Phase-averaged wall-normal velocity fluctuations observed at $x/L = 0.18$ and with upstream PDOS activated at $y_{PDOS}/\delta =$ (a) 0.9%, (b) 3.9%, and (c) 8.7%, and wall- normal velocity fluctuations observed at $x/L = 0.28$ with $y_{PDOS}/\delta =$ (d) 0.9%, (e) 3.9%, and (f) 8.7%.	27

Figure 16. Time-averaged velocity profiles of the baseline case, and three excitation cases of $y_{PDOS}/\delta = 0.9\%$, 3.9% , and 8.7% at (a) $x/L = 0.18$ and (b) 0.28 . The solid line represents the Blasius solution.....	29
Figure 17. Phase-averaged streamwise velocity fluctuation $x/L = 0.28$ with four excitation-control cases (i.e., both PDOS actuators activated) at phase shifts (a) $\Delta\Phi = 0^\circ$, (b) $\Delta\Phi = 90^\circ$, (c) $\Delta\Phi = 180^\circ$, (d) $\Delta\Phi = 270^\circ$, and (e) with only the upstream PDOS activated (excitation).	30
Figure 18. Phase-averaged wall-normal velocity fluctuation at $x/L = 0.28$ with four excitation-control cases (i.e., both PDOS actuators activated) at phase shifts (a) $\Delta\Phi = 0^\circ$, (b) $\Delta\Phi = 90^\circ$, (c) $\Delta\Phi = 180^\circ$, (d) $\Delta\Phi = 270^\circ$, and (e) with only the upstream PDOS activated (excitation).	31
Figure 19. Phase-averaged streamwise velocity fluctuation at $x/L = 0.28$ for three phases along the excitation cycle with the upstream PDOS only (a-c) and both PDOS actuators active (d-f).	33
Figure 20. Phase-averaged wall-normal velocity fluctuation at $x/L = 0.28$ for three phases along the excitation cycle with the upstream PDOS only (a-c) and both PDOS actuators active (d-f).	34
Figure 21. Phase-averaged velocity vector fields at $\phi = 240^\circ$ with (a) excitation only and (b) excitation-control.	35
Figure 22. Wall-normal distributions of the velocity fluctuations for maximum amplitude phase-locked structures of the (a) streamwise component and (b) wall-normal component.....	36
Figure 23. Neutral stability curve (after Kotsonis et al., [44]) with locations of the upstream and downstream PDOS actuators superimposed in red.	38

ACKNOWLEDGMENTS

This work was supported by Northrop Grumman Corporation. Funding for the wind tunnel model and partial support were also provided by the Israel Ministry of Defense.

I would like to acknowledge my advisor, Dr. Michael Amitay, for his significant assistance, guidance, and patience. Without his help, this work would not have succeeded.

I would also like to thank my labmates, both past and present, at the Center for Flow Physics and Control for their scientific expertise and their friendship. In particular, I would like to acknowledge Dr. Edward DeMauro for his teaching and mathematical acumen, Dr. Keith Taylor for his perspective as a fellow physicist-turned-engineer, and Dr. Tyler Van Buren for his initial work developing the PDOS actuator. In addition, Dave Digiulio's machining skills have repeatedly proven indispensable.

I would also like to thank my labmates both past and present: Dr. Chia Min Leong, Karry Rusello, Matthew Boucher, Brian Debronsky, Michael Beyar, Hermanus Van Der Schijff, Dr. Nicholas Rathay, Dr. Joseph Vasile, Jeremy Gartner, Dan Lander, Victor Sivaneri, Marianne Monastero, Samantha Gildersleeve, Erica Cruz, Kevin Housley, Joe Eilert, Thomas Rice, Dr. Burak Ahmet Tuna, Wilfred Chan, William Bugden IV, Danny Moore, Shelby Hayostek, and Dan Spatcher.

I was fortunate to have the help of many undergraduates on this project. I would particularly like to thank Lucia Chang Pikcilingis, Tabitha Bogardus, Mike Tuccio, and Eva Mungai for the significant time that each of them invested in this work.

I am grateful for the friends that have lent their support through all life's trials and tribulations. In particular, I would like to thank Zara Weinberg for her love, mix tapes, and 12+ years of bad jokes. I would also like to thank Robert Altman for his support during my first year of grad school and Jason Gum for his friendship.

I am thankful for my family: Peg Cartano, Lauri Weaver, and Linda Dettbarn, for their love and holiday cards. Receiving your packages always makes me smile.

Last, but never least, I would like to express my love to my parents, Susan Dell'Orso and Rick Heeder. Thank you for your encouragement and unending support.

ABSTRACT

This work characterizes and controls Tollmien-Schlichting (T-S) waves by means of Piezoelectrically-Driven Oscillating Surface (PDOS) actuators, using Particle Image Velocimetry (PIV). A parametric study of PDOS actuator design parameters was conducted and a 0.79 mm thick rubber surface with a 12.7 mm diameter circular dimple, a cavity height of 2 mm, and a neck height of 2 mm was selected for implementation in T-S wave control over a flat plate. Two circular PDOS actuators were used to excite and control the most amplified frequency of the T-S wave on a flat plate. The actuators were placed at the mid-span of a flat plate at two streamwise locations of $x/L = 0.18$ and $x/L = 0.28$ downstream from the leading edge, where the free-stream velocity was $U = 16$ m/s. The upstream actuator was used to excite and phase-lock the T-S waves at an excitation frequency of $f_{act} = 250$ Hz (corresponding to the most amplified frequency of the T-S wave, based on linear stability analysis), and the downstream PDOS was used to mitigate the T-S wave by driving it at an anti-phase with the appropriate amplitude. Time- and phase-averaged flow fields were acquired at two downstream interrogation domains. The first window of data, taken in between the two PDOS actuators, explored the effect of the excitation amplitude on the magnitude of the excited T-S waves. At the second window, located downstream of both PDOS actuators, the simultaneous activation of both actuators at an appropriate phase shift and amplitudes resulted in a significant reduction or augmentation of the T-S waves, depending on the phase shift between the two actuators.

1. INTRODUCTION

Drag associated with skin friction is a significant concern in many aerospace applications. Emerging technologies such as micro-air vehicles must operate at low Reynolds number regimes, where drag is dominated by skin friction drag and it is favorable to maintain a laminar boundary layer over much, if not all, of the vehicle's surfaces. One proposed method for skin friction drag reduction is to use active surface modification to suppress flow instabilities in order to delay transition from laminar to turbulent flow, thus reducing drag.

Two primary types of transition exist. The first type of transition is where small disturbances grow and the flow field, particularly the boundary layer over a surface, gradually transitions to turbulence [1]. The second type of transition occurs when a disturbance to the flow is large enough to bypass these intermediate stages and transition directly to turbulence, i.e., the 'bypass mechanism' [2]. This work focuses on the former. Schlichting & Gersten [1] discussed the transition to turbulence on a flat plate where instabilities start as 2-D waves, known as Tollmien-Schlichting, or T-S waves, which grow and develop three dimensionalities as they propagate downstream. Certain unstable frequencies grow in amplitude, whereas others are known to decay. Linear stability theory can be used to determine stable and unstable eigenmodes which grow and decay, respectively, as they advect downstream [3], [4]. The growth rate for disturbances in the flow can be approximated using the Orr-Sommerfeld equation [5]–[7]. In practice, unstable modes develop nonlinearities, which interact with one another and with the base flow and transition to turbulence. In natural flight, this can be triggered by natural external disturbances like free stream turbulence and sound, or by local disturbances like surface irregularity and vibrations [8].

Prior to the development of nonlinearities, these waves are small in magnitude, (i.e., on the order of 0.1% of the free-stream), which makes them notoriously difficult to

Portions of this chapter previously appeared as: M. Amitay, B. A. Tuna, and H. Dell'Orso, "Identification and Mitigation of T-S Waves using Localized Dynamic Surface Modification," *Phys. Fluids*, vol. 28, no 6, pp. 064103, 2016.

Portions of this chapter also previously appeared as: H. Dell'Orso *et al.*, "Control of Tollmien-Schlichting Waves Using Piezoelectrically Driven Oscillating Surface," in *AIAA Aviation 45th Annual Fluid Dynamics Conference*, Dallas, TX, 2015.

detect with existing non-intrusive measurement techniques. In the early stages of transition (i.e., the linear stage), introducing well-defined and controlled disturbances may be necessary to observe the T-S waves, although a boundary layer subjected to free stream turbulence of greater than 1.5% can be observed without external forcing [9]. As the disturbances propagate downstream, the 2-D waves grow and develop 3-D spanwise waviness. Turbulent spots will develop at a location downstream of the formation of three dimensionalities, and the turbulence introduced at these spots is the final stage before the flow is fully turbulent [1], [2], [10]. Prior work has focused on both naturally occurring T-S waves [8], and forced instabilities [4], [11]–[14], with results of the latter being directly applicable to the former [15].

Under certain circumstances, a large amplitude disturbance is introduced to the flow and the linear regime is bypassed, in a process known as ‘bypass transition’ [10], [16], [17]. In these circumstances, linear theory and the Orr-Sommerfeld equation are not applicable; turbulent spots or subcritical spots cause the flow to quickly transition [10]. This work focuses will focus on the linear regime and attempts to control flow behavior when the bypass mechanism does not occur.

Historically, numerical simulations modeling the transition location assumed parallel flow [6], [7], resulting in a difference between the critical Reynolds number, Re_{crit} , observed by Ross et al. [18] and numerical values calculated by Jordinson [7] and Barry & Ross [19]. Fasel & Konzelmann [20] numerically investigated transition using non-parallel effects without neglecting any terms of the non-linear N-S equation and concluded that using parallel theory as an initial approximation, with the addition of amplitude distributions to account for non-parallel effects, was “well justified”. Fasel & Konzelmann [20] theorize that the difference between experimental and numerical results could have been due, in part, to different authors using different criteria to define transition. Improved transition modeling and experimental techniques have led to very successful agreement between theory and experiment [10].

Receptivity, defined by Lin et al. [21] as, “the process by which external disturbances lead to instabilities in shear flows,” is affected by freestream turbulence, surface roughness, geometry, acoustic noise, vorticity, etc. [10]. Receptivity over a flat plate can change the transition location and, as such, it is important to understand this

factor when exploring the flow physics or developing numerical simulations of transitioning flows. On a flat plate with elliptical leading edge, the Navier-Stokes equations were solved numerically by Lin et al. [21], who found that the sharpness of the leading edge determined the receptivity of the boundary layer to in-plane sound waves. Work on the effect of acoustic disturbances showed that, when coupled with slight pressure changes created by a variable thickness flat plate, they can cause T-S wave magnitude to grow to be the same order as the external disturbance [22], [23]. Crouch found analytically that the Blasius boundary layer is 50 times more receptive to non-localized acoustic disturbances than to localized vortical structures [24]. In addition, the height of micro-sized discrete roughness elements was shown by Hunt & Saric to have a direct impact on the receptivity of flow in a cross-stream [25].

Effects like flow receptivity can be exploited via passive flow control in order to delay the transition to turbulence, with the intent of reducing skin friction drag by increasing the area where the flow is characterized by a laminar boundary layer. Passive flow control is a primarily static approach to flow modification wherein a method of flow control, such as vortex generators or discrete roughness elements, is chosen in advance and implemented in order to reduce overall laminar skin friction drag. However, because this form of flow control cannot be disabled when not required to reduce separation, delay transition, etc., it can create a drag penalty under certain circumstances [26].

Passive flow control targeted at directly affecting T-S waves has been limited. Fransson et al. [27] experimentally used surface roughness elements to generate vortices, inducing streaks in the flow, and found that when the correct surface roughness elements were used, transition was delayed compared to the smooth case. They attributed this to a reduction in the exponential growth rate of T-S waves. More often, vortices are generated by vortex generators rather than dimple-shaped roughness elements, and it is worth noting that the utility of vortex generators is not confined to T-S waves. Among other work, Lin [28] used low-profile vortex generators to reduce separation, Zaman et al. [29] investigated triangular shaped vortex generator “tabs” to control an axisymmetric jet, and work was done on specific vortex generator design by Godard and Stanislas [30].

In contrast to passive flow control, active flow control can be activated when needed to reduce drag, and deactivated when it would impose a drag penalty [26]. It should be noted that, in order for active flow control to be economically viable, the cost of employing the flow control must be significantly less than the amount saved by its operation (as measured in power, fiscal cost, etc.). In order to achieve this, it is necessary to develop a sophisticated understanding of the flow physics before implementing active flow control. In this work, this was achieved through linear stability analysis, as per the works of Gaster, Gaster, and Jordinson, which were used to exploit the characteristic flow frequencies, wavelengths, and phase velocities from which the actuator's characteristics were defined [5]–[7].

Cattafesta & Sheplak [31] discussed 4 types of active flow control: moving object/surface (i.e., vibrating ribbon, morphing surface, oscillating wire, and dynamic surfaces), plasma, fluidic (i.e., jets and synthetic jets), and miscellaneous other (electrohydrodynamic and magnetohydrodynamic). Significant work has been done to mitigate T-S waves in the categories of moving objects and plasma actuators.

Particularly in the case of moving object/surface actuators, the characteristic (most amplified wave) frequency should be used during active flow control [5]–[7]. This frequency can be predicted using linear stability analysis, and control can be enacted using the linear superposition of these waves. That is, when a 2-D Tollmien-Schlichting wave with known phase and amplitude interacts with a disturbance having the same frequency and amplitude (but opposite phase) the result is a significant reduction of the wave amplitude. The first experiment to demonstrate partial wave cancellation was conducted by Wehrmann, wherein a flexible wall was actuated at the anti-phase of the T-S wave, delaying transition [32]. When the flexible wall was applied in-phase with the T-S wave, the magnitude of velocity fluctuations increased [32]. Similar delay was accomplished numerically by Joslin et al., using the nonlinear unsteady Navier-Stokes equations [33], [34]. In addition, experimental work by Thomas [13] actuated one vibrating ribbon on the surface of a flat plate at a frequency associated with an unstable frequency that was predicted numerically. A second, downstream, ribbon at equal amplitude and opposite phase was used to cancel the wave in question. This resulted in a delay of transition but, due an increase in the level of background 3-D disturbances, did

not return the flow to its base state. Thomas believed that returning the flow to a fully laminar state at higher Reynolds numbers would be pragmatically difficult due to the rapid growth of T-S waves under these conditions, but is theoretically possible. Milling used two sequential vibrating wires on a 5.5 m long flat plate in order to change the transition location from 3.3 m downstream of the leading edge of the flat plate to a distance greater than the length of the flat plate itself [11]. Additional experiments were conducted using heaters on a flat plate [12], [35], and via a multi-channel control system with adaptive algorithm on an unswept wing [14].

These works were successful in reducing the velocity fluctuations; however, downstream of the controlling actuator, transition to turbulence may still occur due to the growth of uncontrolled 2-D or 3-D modes. To address this, Opfer conducted an experiment using suction and blowing created by speakers embedded in a flat plate, as well as one with an external loudspeaker that were designed to delay transition by direct adaptive interaction with 2-D and 3-D disturbances [4]. In general, it is easier to control waves when they are in the primarily 2-D regime, as linear numerical techniques can also be 2-D. This was displayed by Losse et al., who used 2-D models to develop a control scheme using the Galerkin model, based on techniques that could be applied to experimental work [36].

Other researchers have used plasma actuators, specifically dielectric barrier discharge (DBD) plasma actuators, for T-S wave control. These actuators are composed of two electrodes, one encapsulated in dielectric material and the other exposed to the surrounding air. When a strong voltage (10-20 kV peak-to-peak AC) is applied, plasma forms above the encapsulated actuator, starting at the leading edge and moving downstream [37]. Typically, DBD plasma actuators generate a body force that couples with the external flow momentum, and have the advantages of being light weight with a fast time response [31], [38]. However, they do require significant driving voltage, i.e., $O(10^3 \text{ V})$ and a power output on the order of 10s of watts [31], [37], [38]. This can limit their applicability for certain aeronautical applications.

Widmann et al. [39] used a vibrating ribbon to phase-lock T-S waves in a method similar to work by Thomas [13], and then captured the flow field's behavior with PIV. This was a direct precursor to the use of a DBD plasma actuator by Duchmann et al. [40]

and Widmann et al. [41], which utilized the same flow field conditions as the experiment by Widmann et al. [39] and actuated the aforementioned DBD plasma actuator at a downstream location. These works sought to reduce the T-S wave and develop insight into the interactions between their actuator and T-S wave behavior. In doing so, the viability of using Particle Image Velocimetry (PIV) to observe T-S waves and their cancellation was demonstrated, and Duchmann et al. reported a 26% reduction in T-S wave magnitude directly downstream of the actuator [40].

Other boundary layer reduction work conducted using DBD plasma actuators include experimental work by Grundmann & Tropea who used an electromagnetic turbulator, i.e., a type of vibrating surface driven by a square wave AC voltage, to excite the T-S wave [42], [43]. Subsequently, both pulsed and steady downstream plasma actuators were used to reduce the wave's amplitude. Additionally, Kotsonis et al. used the unsteady 2-D Navier-Stokes equations to model the effect of plasma actuator control on T-S waves [44].

It should be noted that closed-loop control of T-S waves has also been achieved using the superposition principle. In this method, a non-intrusive reference sensor is required to detect the T-S waves, which are cancelled farther downstream using an actuator. Specifically, Sturzebecher & Nitsche [14] and Engert et al. [45] explored natural T-S waves on an unswept wing, which were reduced through the use of an adaptive control algorithm. Spanwise arranged sensor-actuator systems were employed to provide mitigation of 3-D waves. Additional closed-loop control via DBD plasma actuators was investigated by Kurz et al. [46] and Barckmann et al. [47]. Closed-loop systems and/or those with optimization algorithms like the ones investigated by de Quadros et al. [48] offer improved T-S wave mitigation over manually determined control techniques, and are the ultimately preferred method. Nevertheless, demonstrating the feasibility of a novel actuator (such as the one described in the present work) is best accomplished prior to implementing closed-loop control.

Other actuators are also under development for active flow control applications. Recently, dynamic roughness elements, a subset of moving surface actuators, have also experienced an increase in related research. Electro-active polymers (EAPs), discussed by Dearing et al. [49], are formed from an elastomer attached to a substrate and

sandwiched between two compliant electrodes, with an array of pockets cut into it. When an external voltage is applied, the electrostatic force causes the elastomer to expand into the pocket creating a dimple. When an AC current is used, the elastomer fluctuates at the given frequency, adding vorticity to the flow. Van Buren and Amitay [50] used EAPs to trigger transition, and theorized that a similar device could be used to delay transition. DeMauro et al. [51] followed this by using EAPs to reduce the extent of a separation bubble on a NACA0009 airfoil. They also noted that the presence of slight surface roughness from the unactuated EAPs had an observable effect on the magnitude of the same separation bubble.

The present work seeks to build on previous success in T-S wave mitigation by applying linear superposition of waves using discrete oscillating surfaces. Specifically, this will be enacted using two Piezoelectrically-Driven Oscillating Surface (PDOS) actuators. There is an established precedent of successfully using oscillating surfaces to reduce skin-friction drag in non-T-S wave situations such as separation bubbles, separation delay, and variable-cambered airfoils. Rist & Augustin [52] numerically demonstrated that small, unsteady dynamically oscillating surface disturbances are sufficient to control laminar separation bubbles, and they stated that using actuation frequencies that correspond to the characteristic flow frequency for control is more effective than steady/passive disturbances. Pinkerton & Moses [53] experimentally studied an active flow control mechanism and delayed boundary layer separation by actively altering the airfoil camber. More recently, Abdullah et al. [54] investigated use of shape-memory alloys as a means of creating variable-camber airfoils. Udovitchik & Morrison [55] showed the ability of surface-mounted unsteady dimples to delay boundary layer separation on a cylinder, demonstrating the effectiveness of discrete roughness oscillating surfaces as a form of flow control.

However, the idea of applying a discrete roughness oscillating surface to control T-S wave development is a different approach. This work aims to control T-S waves on a flat plate by investigating the feasibility of a novel actuator, i.e., the PDOS actuator. Specifically, two PDOS actuators are used at two downstream locations: the upstream actuator is placed such that for a given Reynolds number it is at the most amplified region of the neutral stability curve, whereas the downstream actuator is located in the

non-amplified region, as calculated based on the work of Jordinson [7] and Kotsonas et al. [44]. The intent of this is to phase-lock the T-S wave and allow it to grow in the linear regime, and then cancel it in the non-amplified regime so that the mitigated wave will not grow again as it is advected downstream. Other work using this approach is limited [56] [57]. Preliminary investigation using EAP actuators was the impetus for the development and implementation of the PDOS actuator, and is also discussed.

2. ACTUATOR DESIGN AND QUANTIFICATION

2.1 EAP Actuator Quantification and Testing

Preliminary work evaluated the possibility of using electro-active polymer (EAP) actuators as a form of active flow control for T-S wave control. Figure 1 shows the EAP actuator, which is constructed from a dielectric elastomer material sandwiched between two compliant electrodes. When exposed to a potential difference, the elastomer changes its shape, expanding into the pocket [49]. When a time-variant voltage is applied, periodic deflections are created; the voltage applied determines the amplitude of the deflection. The maximum diameter and height of dimples are constrained by the diameter and height of the pockets used in the actuator.

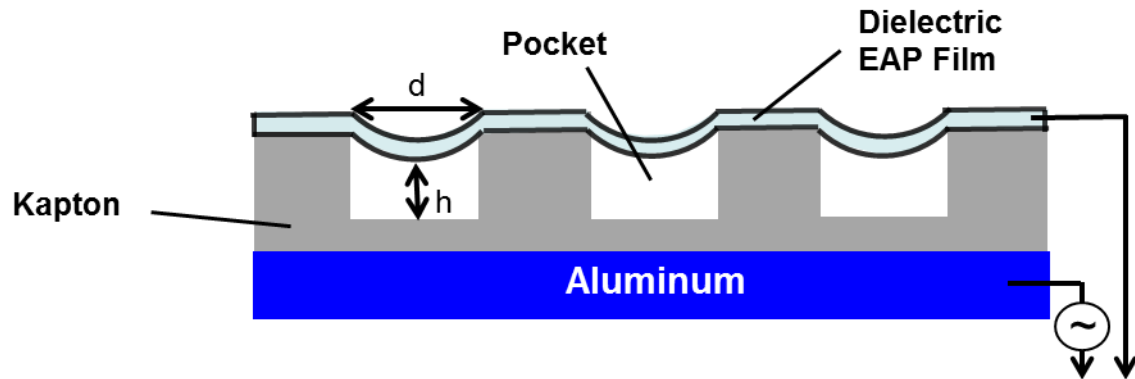


Figure 1. Schematic of an EAP actuator.

Figure 2 shows the EAP actuator before and after deflection. Prior to actuation (Figure 2a), the surface of the elastomer is smooth with slight elements of surface roughness. It is believed, based on the results of DeMauro et al. [51], that the presence of this slight surface roughness does impact the flow field. The PDOS actuator, discussed in more detail below, does not have this issue. After actuation (Figure 2b), the EAP's elastomer deflects in the pockets, creating well-defined dimples. It should be noted that the elastomer only deflects into the pocket; using this actuator, it is not possible to create raised dimples.



Figure 2. EAP actuator (a) before and (b) after an external voltage difference is applied.

As mentioned previously, the depth of the pockets (here, 0.2 mm) is the upper constraint of dimple height. In addition, peak-to-peak deflection is also a function of external frequency and voltage. Although peak-to-peak deflection varied slightly between dimples, a representative quantification was obtained. Figure 3 shows dimple deflection for voltages between 0 and 2500 V, which is the upper limit of the actuator, and frequencies from 1 to 500 Hz. For actuation frequencies above 500 Hz, the oscillations of the elastomer are minimal. At the lowest actuation frequency, 1 Hz, the actuator's maximum deflection is 0.087 mm, which is significantly less than the 0.2 mm maximum imposed by the pocket depth. Unfortunately, as Figure 3 shows, at higher actuation frequencies the peak-to-peak motion of the EAP actuator decreases. At 200 Hz (which is close to the characteristic frequency used in this work), the maximum achievable displacement is a mere 0.018 mm.

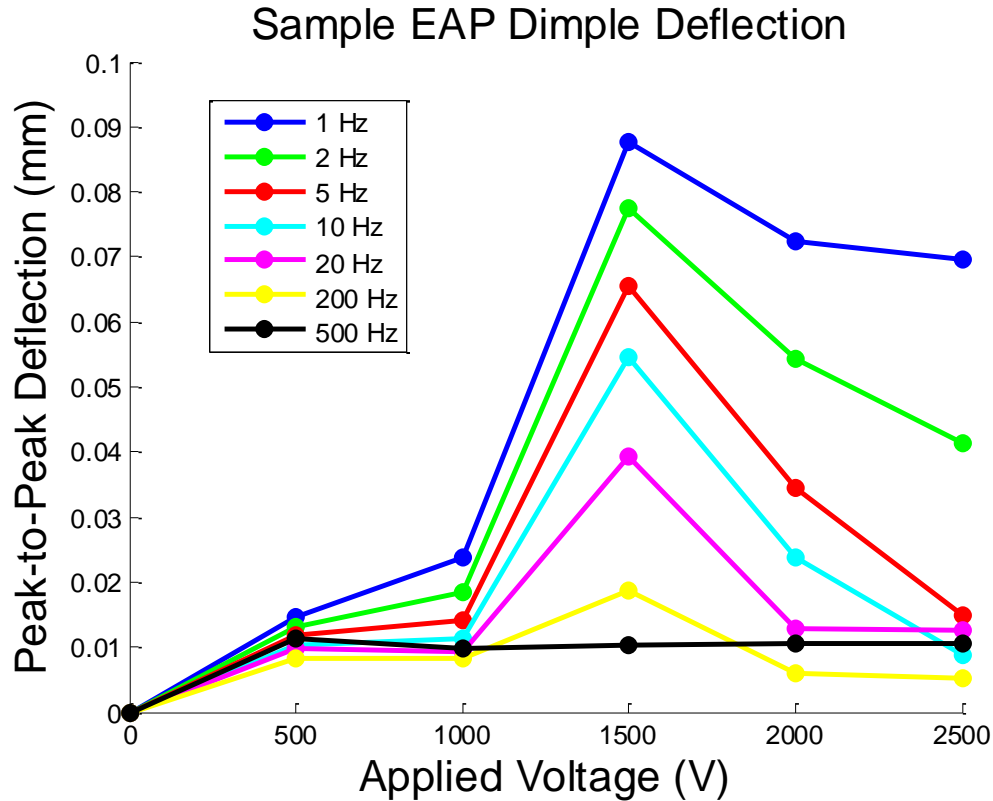


Figure 3. EAP dimple peak-to-peak deflection for frequencies from 1 Hz to 500 Hz.

During actuation, the peak-to-peak motion of EAP dimples is dependent on the driving frequency and voltage. However, the maximum displacement did not exhibit a strong dependence on driving voltage, as shown in Figure 4b. This is due to the fact that when an external voltage is applied to the EAP actuator it causes the elastomer to deflect slightly into the cavity, relative to the flush position shown in Figure 2a. This new ‘home’ position is referred to as the DC offset, and is a function of the applied frequency and voltage. Figure 4a shows the relationship between DC offset and driving voltage. Higher frequencies yielded higher DC offsets for a given voltage, limiting the peak-to-peak motion that is possible for higher frequencies. Since flow control of T-S waves is exercised primarily through the dynamic motion of the dimples, this behavior severely curtails the effectiveness of the EAP actuator.

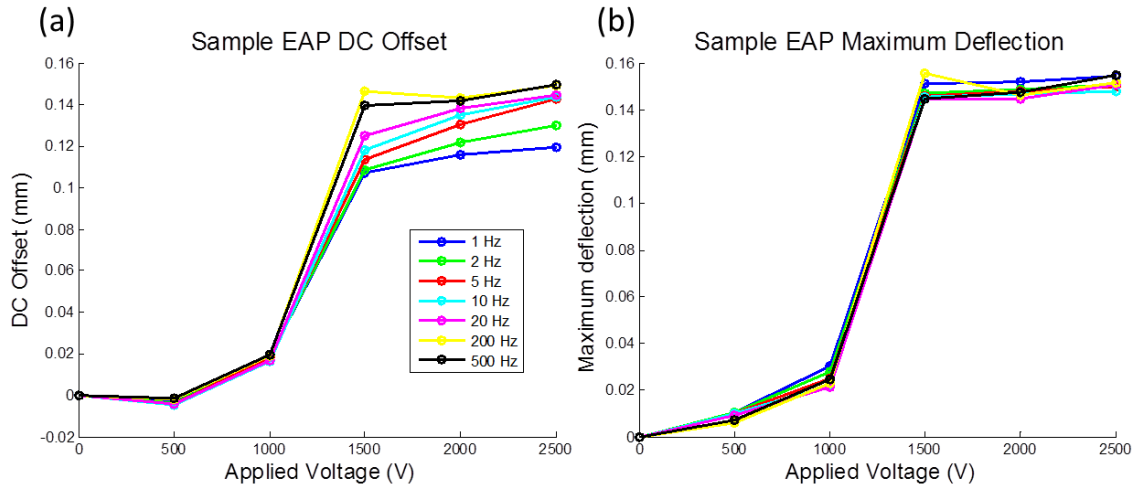


Figure 4. EAP dimple (a) DC offset and (b) maximum deflection for frequencies 1 Hz to 500 Hz.

Preliminary wind tunnel testing demonstrated that peak-to-peak motion of the EAP actuator is not sufficient to control T-S waves at the frequency required (250 Hz). Therefore, it was necessary to develop an alternative control method, which could provide greater dynamic motion for T-S wave control. To accomplish this, the PDOS actuator was designed, quantified, and ultimately employed for transition control.

2.2 PDOS Actuator Design and Quantification

Each PDOS actuator was designed to create a discrete dimple via a dynamic rubber surface for use in active flow control. An exploded view of the actuator is shown in Figure 5. For quantification purposes, the actuator was mounted to an optical table using the setup shown in Figure 5. This piece was attached to the remaining assembly via 6 equally spaced 8-32 screw holes using torque $\tau = 11$ in-lbs. A pre-stressed piezoelectric disk, shown in Figure 5 as the gold plate, was adjacent to the mounting plate. When an AC voltage is applied at a specific frequency and amplitude, it causes the piezoelectric disk to oscillate at that frequency and at a voltage-dependent maximum amplitude. This, in turn, creates an oscillating motion on the rubber surface, which is the control surface for the actuator. The amplitude of the rubber oscillations is determined by the magnitude of the piezoelectric disc, coupled with the effects of cavity and neck sizes.

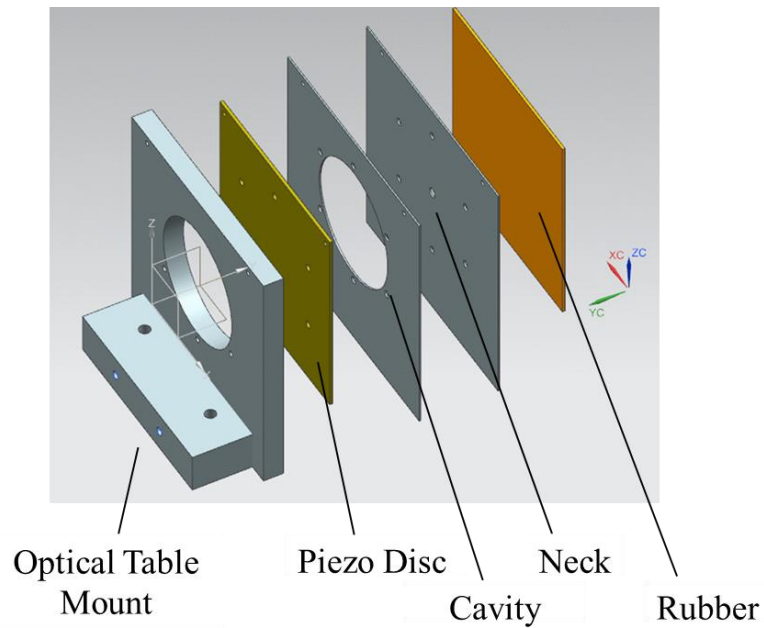


Figure 5. Exploded view of PDOS actuator used for optical table quantification.

The piezoelectric disk used in the PDOS actuator, shown in Figure 6, is a specially designed pre-stressed bimorph piezoelectric wafer and is composed of two unimorph PZT 5A wafers with a plastic substrate in between. A protective coating was applied to encapsulate the bimorph. Leads were applied to each of the four soldering pads (shown in the upper part of Figure 6) in order to apply the AC voltage.

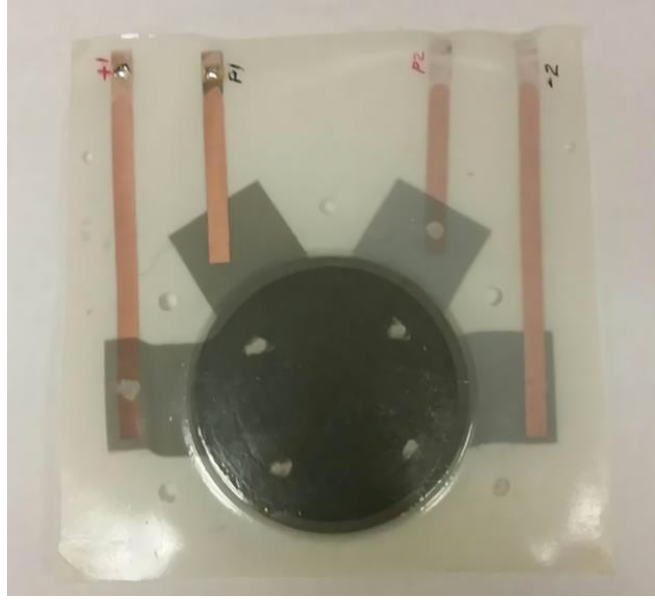


Figure 6. Piezoelectric disk used in the PDOS actuator.

The maximum combined heights of the neck and cavity were dictated by the physical limitations of the wind tunnel flat plate model (7 mm) and the diameter of the cavity (79.4 mm) was chosen based on the diameter of the piezoelectric disk. In order to quantify the performance of the PDOS actuator (i.e., measure peak-to-peak displacement of the rubber and piezoelectric surfaces surface at various frequencies and amplitudes), the model shown in Figure 5 was mounted to an optical table. Two Keyence laser displacement sensors (LK-402 and LK-82) were used to quantify the deflection of the piezoelectric disk and the rubber, respectively; the complete setup is shown in Figure 7. The laser displacement sensors, which can measure at a rate of up to 20 kHz, were placed at the centers of the rubber and the piezoelectric disk during deflection.

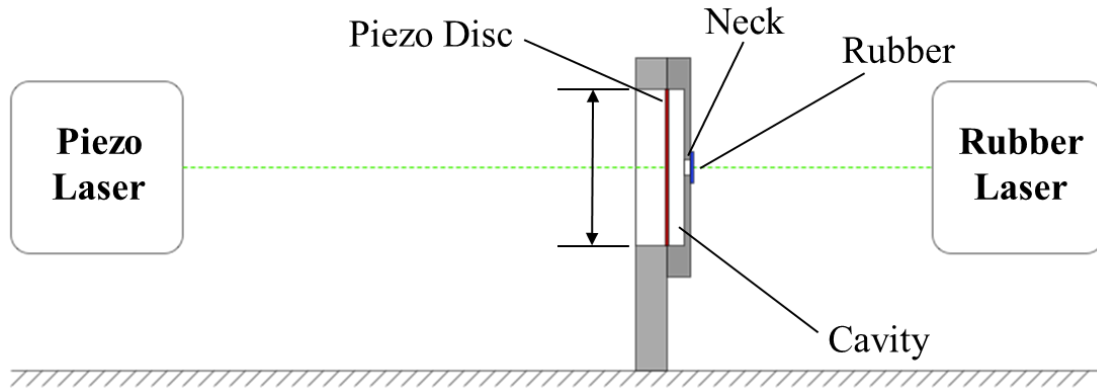


Figure 7. Setup of laser displacement sensors and PDOS actuator for optical table quantification.

A parametric study was conducted to quantify piezoelectric disk and rubber displacements for a variety of configurations of neck shape, rubber thickness, and neck height. The results for quantification of rubber thickness and cavity shape are shown in Figure 8. Peak-to-peak deflection of the rubber, as measured by the LK-82 (which has a measurement accuracy of $0.5 \mu\text{m}$) is shown on the vertical axis; applied voltage is shown on the horizontal axis. All quantification tests were run at 250 Hz, which is the most amplified frequency of the T-S wave for the wind tunnel conditions used in this experiment. In Figure 8, filled in circles represent the thicker rubber (0.79 mm) and plus signs represent thinner rubber (0.39 mm). These thicknesses were selected based on what was commercially available. Dimples with 12.7 mm circular diameter (blue), 6.35 mm circular diameter (green) and 6.35 mm x 2 mm slot (red) are shown. It was found that for both thicknesses of rubber, the largest dimple (12.7 mm circular diameter) showed definitively higher peak-to-peak motion than either the 6.35 mm x 2 mm slot or the 6.35 mm circular diameter dimple. In addition, all orifice shapes showed quasi-linear growth in peak-to-peak deflection, relative to increasing voltage. Of all tested configurations, the thicker ultra-strength neoprene rubber (0.79 mm thick) with 12.7 mm dimple diameter showed the highest deflection; as such, these parameters were selected for wind tunnel testing.

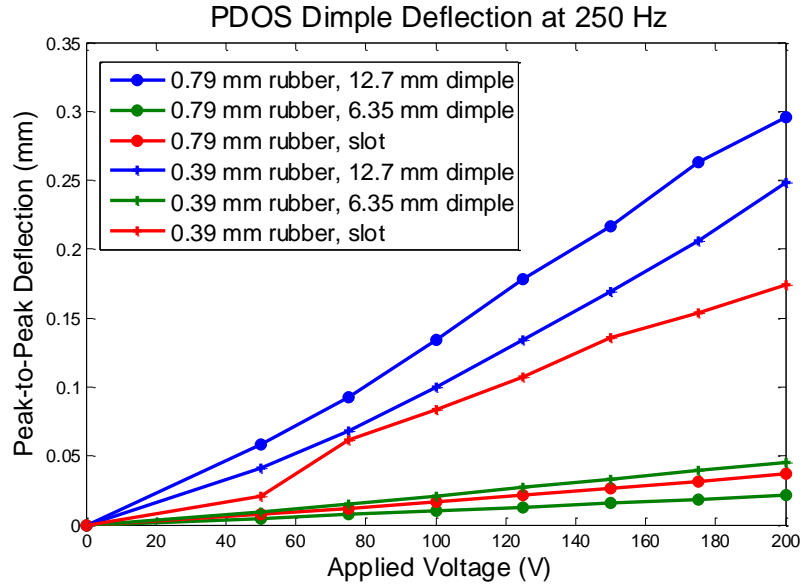


Figure 8. Peak-to-peak rubber deflection for 0.79 mm and 0.39 mm thick rubber surfaces with circular dimples of 12.7 mm and 6.35 mm diameter, and for slot with dimensions 6.35 x 2 mm.

Figure 9 shows dimple deflection based on driving voltage for three different neck heights: 2 mm (red), 3 mm (green), and 4 mm (blue). All three cases showed a linear relationship between driving voltage and peak-to-peak deflection for a given neck height. The shortest neck length, 2 mm, showed the highest peak-to-peak motion, followed by the 4 mm neck length, and then the 3 mm neck length. The order of these deflections is surprising, and it is theorized that it is due to resonance between the motion of the piezoelectric disk and the combined volumes of the cavity and neck in the actuator assembly.

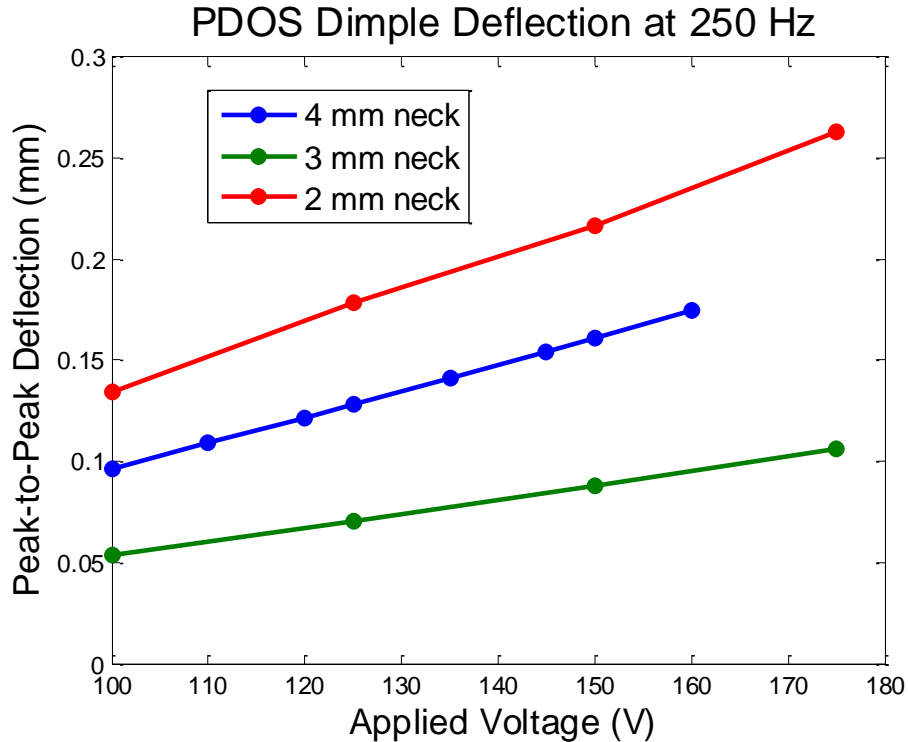


Figure 9. Peak-to-peak rubber deflection for neck heights ranging from 2 to 4 mm.

For wind tunnel testing, ultra-strength, smooth finish, 0.79 mm thick neoprene rubber with 50 A durometer (hardness) was selected. The chosen cavity diameter was 79.4 mm with height 4 mm; the neck was circular-shaped with a diameter of 12.7 mm and height 2 mm. The effect of frequency was tested for the final configuration and can be seen in Figure 10. At the range of frequencies tested, the rubber deflection increased quasi-linearly as the input voltage was increased for all input frequencies. As mentioned previously, the amplitude of the rubber deflection was quasi-linearly proportional to the input voltage amplitude; this appears to be true regardless of neck height, driving frequency, or rubber thickness for the range of conditions tested (Figures 8-10). In addition, for all conditions tested, an increase in driving frequency caused a corresponding increase in the slope of peak-to-peak deflection relative to driving voltage. Note that for the most amplified frequency of the T-S wave (250 Hz, shown in Figure 10 in red), focused on in the present work, the change in the peak-to-peak displacement magnitude varied as approximately: $Displacement = 0.0012 \times Input\ Voltage$.

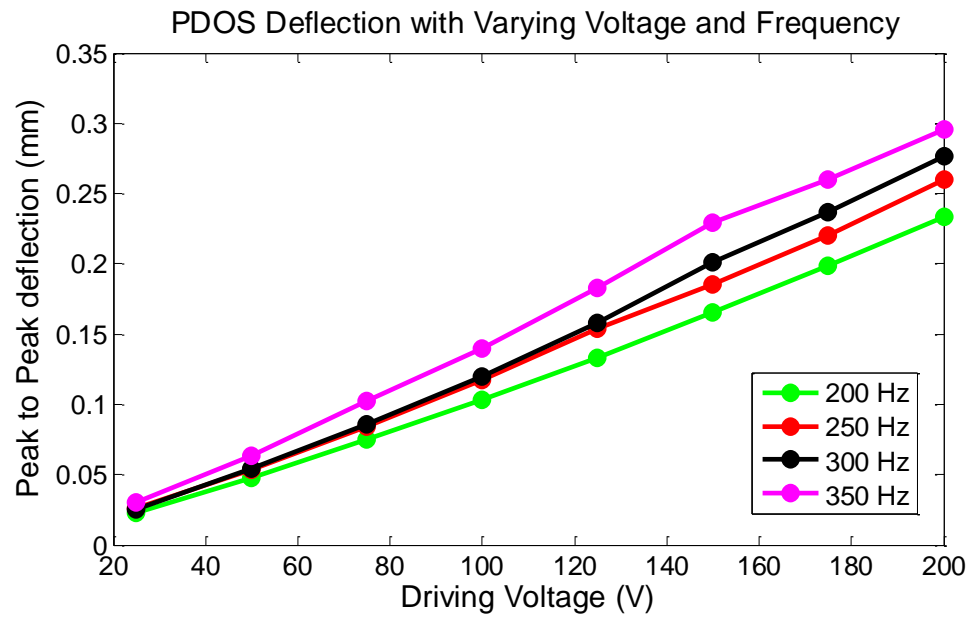


Figure 10. Rubber deflection for the PDOS actuator used in wind tunnel testing.

3. EXPERIMENTAL SETUP AND TECHNIQUES

Wind tunnel testing was performed in the open-return low-speed wind tunnel facility at Rensselaer Polytechnic Institute's Center for Flow Physics and Control (*CeFPaC*). The wind tunnel has a test section with a 0.8 m x 0.8 m cross-section, is 5 m long, and has a maximum speed of 50 m/s, without accounting for blockage effects. Upstream of the test section, the flow passes through a flow conditioning unit, which includes honeycombs and screens to yield a free-stream turbulence intensity of 0.2%. The wind tunnel has a contraction rate of 9:1. The test section walls were made from acrylic to allow optical access during the experiments.

The model used was a flat plate with a streamwise length $L = 1200$ mm, width $b = 610$ mm, and thickness $t = 19$ mm. The flat plate was mounted at mid-height within the wind tunnel test section and between two vertical walls that were connected to the wind tunnel floor, in order to ensure that the experiments were performed in absence tunnel wall effects. A picture of the complete wind tunnel experimental setup is given in Figure 11 and a detailed schematic with side and plan views are given in Figure 12. The flat plate was created with a modular design to allow for easy assembly and future incorporation of different actuation systems. Several pieces of SLA were printed and joined together to form the 4:1 elliptical leading edge of the flat plate as shown in Figure 11a. Note that the length of the flat plate ($L = 1200$ mm) does not include the elliptical leading edge. The SLA pieces were attached to two joined aluminum pieces, followed by an adjustable sharp trailing edge with length 0.101 m that served as a flap to adjust the location of the stagnation pressure at the plate's leading edge. PDOS actuators were mounted into the centerline of the flat plate such that the rubber control surfaces of the actuators were flush with the surrounding aluminum.

Portions of this chapter previously appeared as: M. Amitay, B. A. Tuna, and H. Dell'Orso, "Identification and Mitigation of T-S Waves using Localized Dynamic Surface Modification," *Phys. Fluids*, vol. 28, no 6, pp. 064103, 2016.

Portions of this chapter also previously appeared as: H. Dell'Orso *et al.*, "Control of Tollmien-Schlichting Waves Using Piezoelectrically Driven Oscillating Surface," in *AIAA Aviation 45th Annual Fluid Dynamics Conference*, Dallas, TX, 2015.

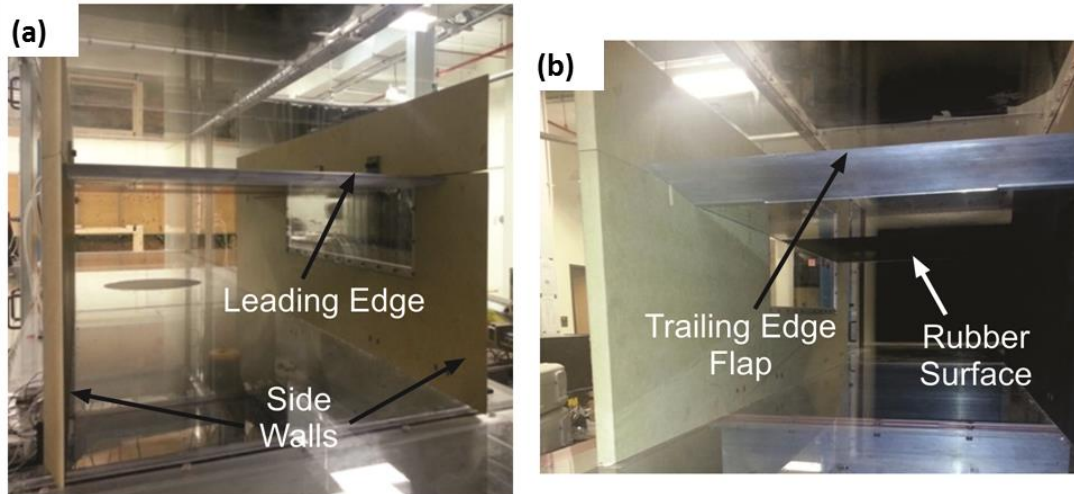


Figure 11. Picture of the flat plate wind tunnel setup looking from the (a) leading edge and (b) trailing edge.

Figure 12 shows the locations of the actuators on the flat plate. The streamwise location of the upstream PDOS actuator relative to the leading edge of the flat plate was set to $L_{us} = 192$ mm ($x/L = 0.16$). The second PDOS actuator was located 115 mm downstream from the upstream PDOS, i.e., $L_{ds} = 307$ mm ($x/L = 0.26$).

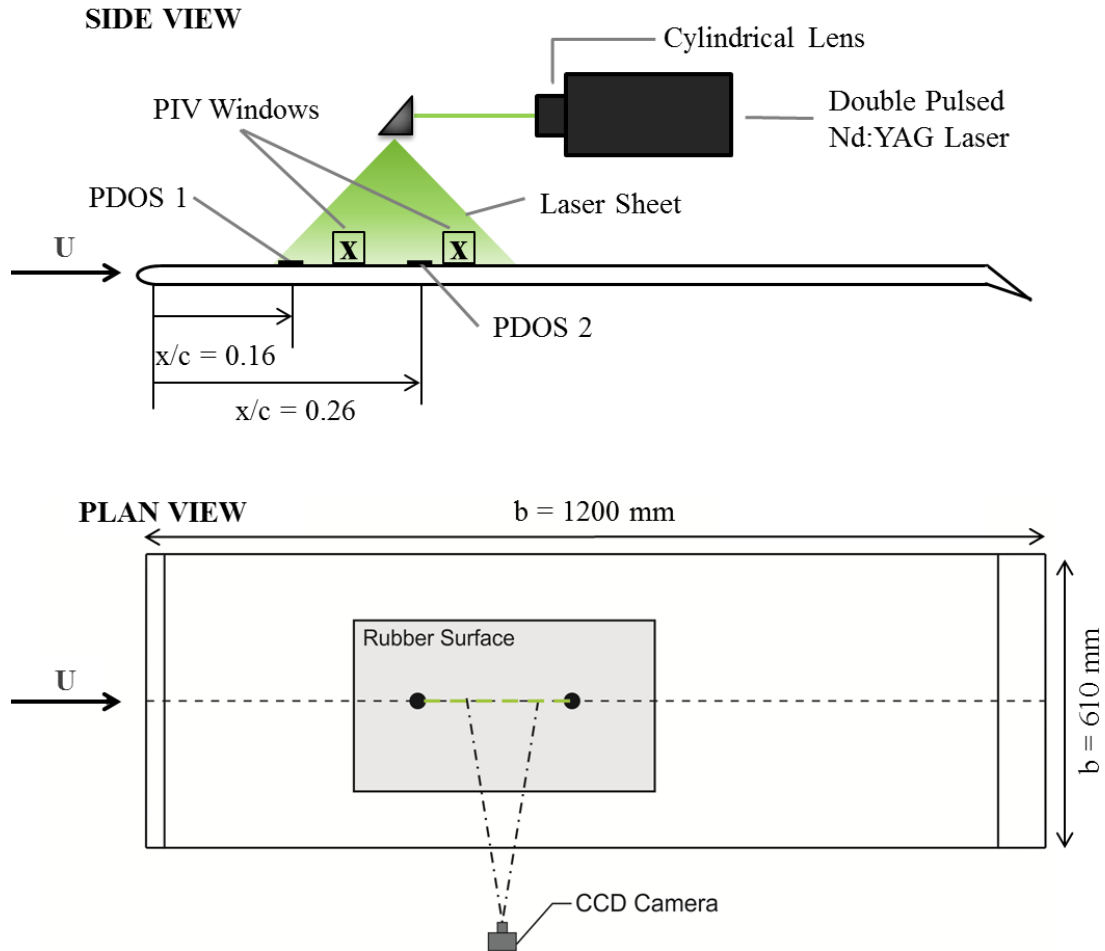


Figure 12. Experimental setup used for wind tunnel testing.

For all experiments described herein, the free-stream velocity was held fixed at $U = 16$ m/s. The boundary layer profile of the baseline flow (i.e., when the PDOS actuators were present but not activated) was obtained using Particle Image Velocimetry (PIV) measurements.

The primary measurement technique used in the present work was PIV, which led to quantitative determination of the flow patterns. The system included a dual pulsed Nd:YAG laser having a maximum output of 120 mJ/pulse, 1,376 x 1,040 pixel resolution thermo-electrically cooled 12-bit LaVision Imager Intense CCD camera, and a programmable timing unit. A -50 mm cylindrical lens was used to create the light sheet in conjunction with a focal lens to focus the sheet at the mid-span of the flat plate to a thickness of about 1 mm at its waist. A 200 mm focal length lens was used in conjunction with a 532 nm \pm 10 nm band-pass filter on the camera in order to acquire

data in the streamwise oriented plane at the plate's mid-span. The laser was positioned underneath the wind tunnel parallel to the flow direction and was allowed to shine through the plexi-glass floor of the test rig, illuminating water-based smoke particle seeding. The CCD camera was mounted perpendicular to the free-stream direction, i.e., the camera was placed on the side of the wind tunnel (the PIV setup is presented in Figure 12). The flow was seeded with $\sim 1 \mu\text{m}$ diameter smoke particles, generated by a theatrical fog machine. The smoke was injected into the tunnel upstream of the test-section through the blower inlet in order to allow it to fully mix and become uniformly distributed at the measurement domain.

Using the aforementioned laser and camera arrangement at the PIV window locations indicated in in Figure 12, 2,500 image pairs were acquired for each case to produce the time- and phase-averaged vector fields. A time delay of $\Delta t = 9 \mu\text{s}$ was applied between successive laser pulses in order to compute the velocity components (U and V) by using the cross-correlation of pairs of successive images. The images were processed using an advanced multi-pass method where the initial and final correlation passes were 64×64 pixels with 50% overlap and 32×32 pixels with 75% overlap, respectively. This technique resulted in 22,663 vectors with a grid size of 0.18 mm, and the effective magnification of the camera provided a resolution of 43.8 pixels/mm.

The time-averaged flow field was obtained by acquiring image pairs throughout the PDOS actuation cycle, and thus included the averaged flow field, random fluctuations, and coherent motions corresponding to the excited T-S wave. In order to isolate the coherent T-S wave fluctuations, $(u_{TS})_p$, which are on the order of 0.1% of the free-stream, it is necessary to filter out random fluctuations. To accomplish this, a trigger signal (associated with the waveform used to activate the upstream PDOS) was used as a reference to obtain phase-averaged data for 6 different phases ($\phi = 0^\circ$ to 300° in increments of 60°) during the actuation cycle of the PDOS. The T-S wave patterns were resolved by subtracting the time-averaged flow field, \bar{U} , from the phase-averaged flow field, U_ϕ :

$$(u_{TS})_p = U_\phi - \bar{U} \quad (1)$$

In order to obtain the growth of the excited T-S wave, PIV data were taken at 2 windows: downstream of the first PDOS actuator, centered at $x/L = 0.18$, and downstream of both PDOS actuators, centered at $x/L = 0.28$. Three different actuation voltages were used, corresponding to peak voltages of 25 V, 100 V, and 200 V, at a frequency of 250 Hz. This frequency corresponds to the most amplified frequency of the Tollmien-Schlichting waves. Note that linear stability analysis (using the experimental velocity profile) was conducted, and is discussed in the Results section. The magnitudes of peak-to-peak displacement of the PDOS for the input voltages used were 0.026 mm ($y_{PDOS}/\delta = 0.9\%$), 0.118 mm ($y_{PDOS}/\delta = 3.9\%$), and 0.260 mm ($y_{PDOS}/\delta = 8.7\%$), respectively, where δ is the boundary layer thickness at $u = 0.99U$ for the baseline case and y_{PDOS} is the maximum wall-normal peak-to-peak displacement of the PDOS.

4. RESULTS

Linear stability analysis performed in the present work on the baseline experimental data showed that the most amplified frequency of T-S waves under these conditions is 250 Hz, which was used to activate the PDOS actuators. Note that previous studies obtained the same frequency [39], [41].

First, the boundary layer was measured and compared to the theoretical Blasius solution to verify that the boundary layer is indeed laminar. Figure 13 presents the Blasius profile in black, plotted in conjunction with measured (using hotwire) and simulated velocity profiles slightly downstream of the first PDOS at $x/L = 0.18$. The simulated data were obtained by Joe Eilert as part of his Master's degree project, in 2015. Clearly, the experimental profile agrees well with both the computational result and the Blasius solution, suggesting that the incoming boundary layer is laminar with a negligible pressure gradient.

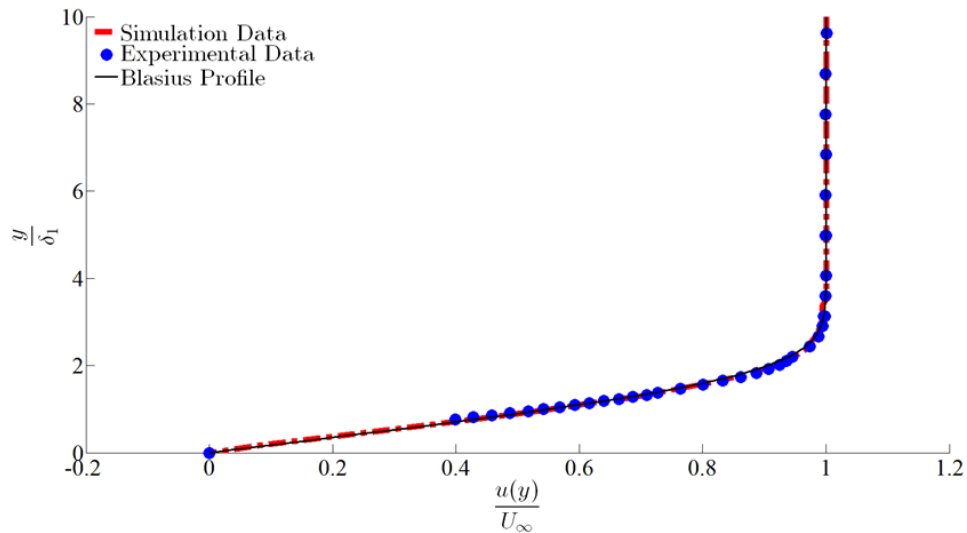


Figure 13. Boundary layer profiles of the experimental data, the Blasius solution, and simulation results (obtained by Joe Eilert).

Portions of this chapter previously appeared as: M. Amitay, B. A. Tuna, and H. Dell'Orso, "Identification and Mitigation of T-S Waves using Localized Dynamic Surface Modification," *Phys. Fluids*, vol. 28, no 6, pp. 064103, 2016.

Portions of this chapter also previously appeared as: H. Dell'Orso *et al.*, "Control of Tollmien-Schlichting Waves Using Piezoelectrically Driven Oscillating Surface," in *AIAA Aviation 45th Annual Fluid Dynamics Conference*, Dallas, TX, 2015.

As mentioned previously, the flow field behavior was measured using PIV, which was then used to isolate Tollmien-Schlichting waves. Since the magnitude of the T-S waves is on the order of 0.1% of the free-stream velocity, in order to capture these structures the coherent velocity fluctuations, $\langle u' \rangle$, were obtained by subtracting the time-averaged velocity field, \bar{U} , from the velocity field at a particular phase, U_ϕ , based on the relationship: $\langle u' \rangle_p = U_\phi - \bar{U}$. PIV data were taken when the upstream PDOS actuator was activated at three driving voltages of 25 V, 100 V, and 200 V (creating maximum peak-to-peak deflections of $y_{PDOS}/\delta = 0.9\%$, 3.9% , and 8.7% , respectively) at streamwise locations $x/L = 0.18$ and $x/L = 0.28$.

Phase-averaged streamwise velocity fluctuations $\langle u' \rangle_p/U$ are shown in Figure 14 for phase $\phi = 0^\circ$ of the actuation cycle of the upstream PDOS. Green color indicates velocity fluctuations moving in the positive streamwise direction (downstream) and blue indicates velocity fluctuations moving in the negative streamwise direction (upstream). The vertical axis is the wall-normal direction non-dimensionalized by boundary layer thickness δ . The horizontal axis is labeled by two scales: the upper scale is the streamwise distance normalized by the boundary layer thickness, δ , and the lower scale is the streamwise distance normalized by the T-S wavelength, λ . Color contours of the phase-averaged streamwise velocity fluctuations are displayed in Figures 14a and d, 14b and e, and 14c and f display at actuation levels of $y_{PDOS}/\delta = 0.9\%$, 3.9% , and 8.7% , respectively. At the lowest actuation level the structures do not appear clearly, particularly at the upstream location (Figure 14a). Moreover, due to the low level of coherent fluctuations and reflections from the surface, the coherent fluctuations near the wall are particularly poorly defined. As the actuation level is increased to $y_{PDOS}/\delta = 3.9\%$ (Figure 14b and e), the magnitude of the coherent fluctuations increases to $\approx 0.5\% U$. The structures are well defined, coherent, and grow as expected in both intensity and physical size as they advect downstream. For the largest actuation level used here, at $x/L = 0.18$ ($y_{PDOS}/\delta = 8.7\%$, Figure 14c), the magnitude of the coherent structures is $\approx 5\% U$ and the structures already appear to be interfering with one another. This phenomenon is exacerbated at $x/L = 0.28$ (Figure 14f), where the structures have grown and possess a magnitude and intensity sufficient to alter behavior outside the boundary layer. This level of actuation yields a non-linear behavior, which will be discussed in Figure 16.

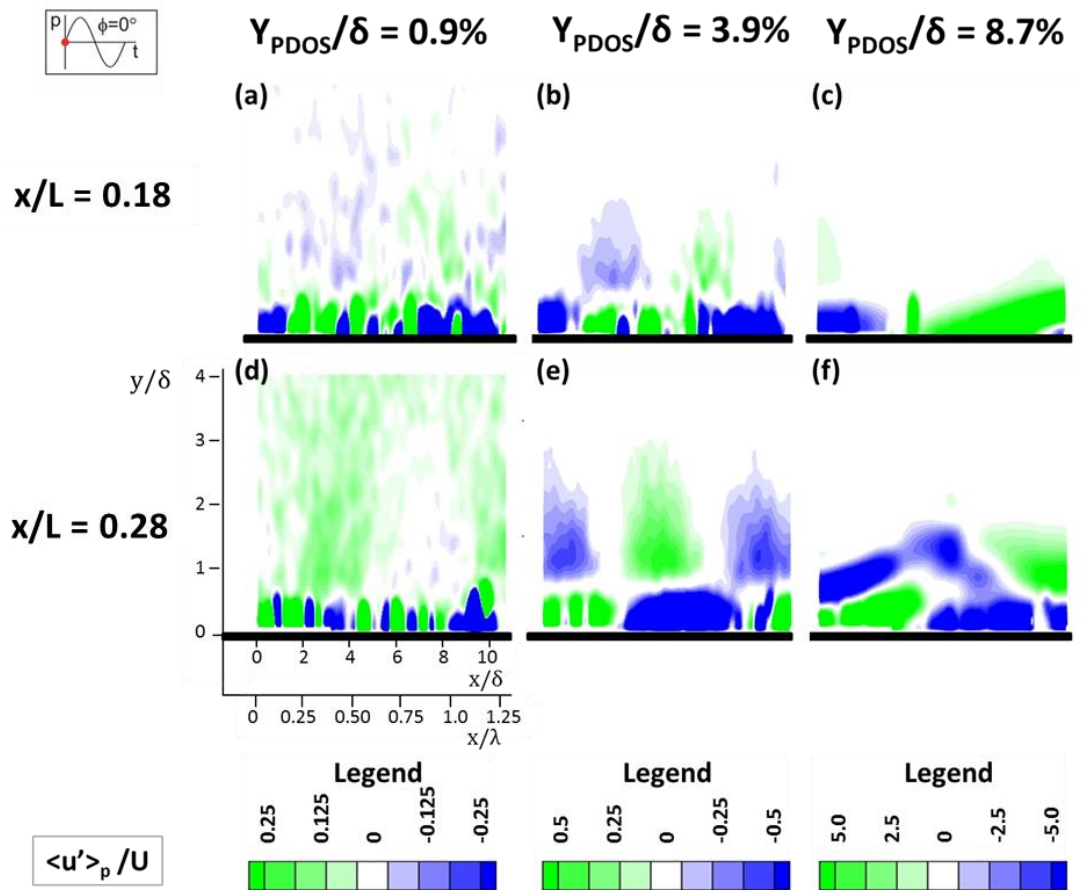


Figure 14. Phase-averaged streamwise velocity fluctuations observed at $x/L = 0.18$ and with upstream PDOS activated at $y_{PDOS}/\delta =$ (a) 0.9%, (b) 3.9%, and (c) 8.7%, and wall-normal velocity fluctuations observed at $x/L = 0.28$ with $y_{PDOS}/\delta =$ (d) 0.9%, (e) 3.9%, and (f) 8.7%.

Similar to the streamwise velocity fluctuations, the normalized phase-averaged wall-normal velocity fluctuations, $\langle v' \rangle_p / U$, were calculated and are shown in Figure 15 at phase $\phi = 0^\circ$. Red color indicates velocity fluctuations moving in the positive wall-normal direction (away from the flat plate) and blue indicates velocity fluctuations moving in the negative wall-normal direction, i.e., toward the flat plate. Figure 15a and d shows the fluctuations when the PDOS actuation level is $y_{PDOS}/\delta = 0.9\%$. At this actuation level the wall-normal coherent fluctuations are better defined than their streamwise counterparts, and appear flame-like, stretching from the surface into the free-stream. The height of these structures increases from 2.5δ to 4δ between the first and second streamwise locations. Moreover, their magnitude increases, as expected.

Figure 15b and e shows the coherent wall-normal fluctuations at $x/L = 0.18$ and at $x/L = 0.28$ when the actuation level was increased to $y_{PDOS}/\delta = 3.9\%$. Structures appear better defined as they advect downstream, increasing in magnitude and physical size in the same manner as the streamwise fluctuations. As coherency improves, the structures lose their flame-like appearance, becoming more clustered. Finally, as the actuation level is increased to $y_{PDOS}/\delta = 8.7\%$, at $x/L = 0.18$, the intensity of the wall-normal coherent structures is $\approx 2\% U$, whereas at the $x/L = 0.28$ location, the measureable physical size of the structures has increased dramatically. As an apparent result of their size and interference with one another, these structures appear distorted and are not as well defined as those at $y_{PDOS}/\delta = 3.9\%$.

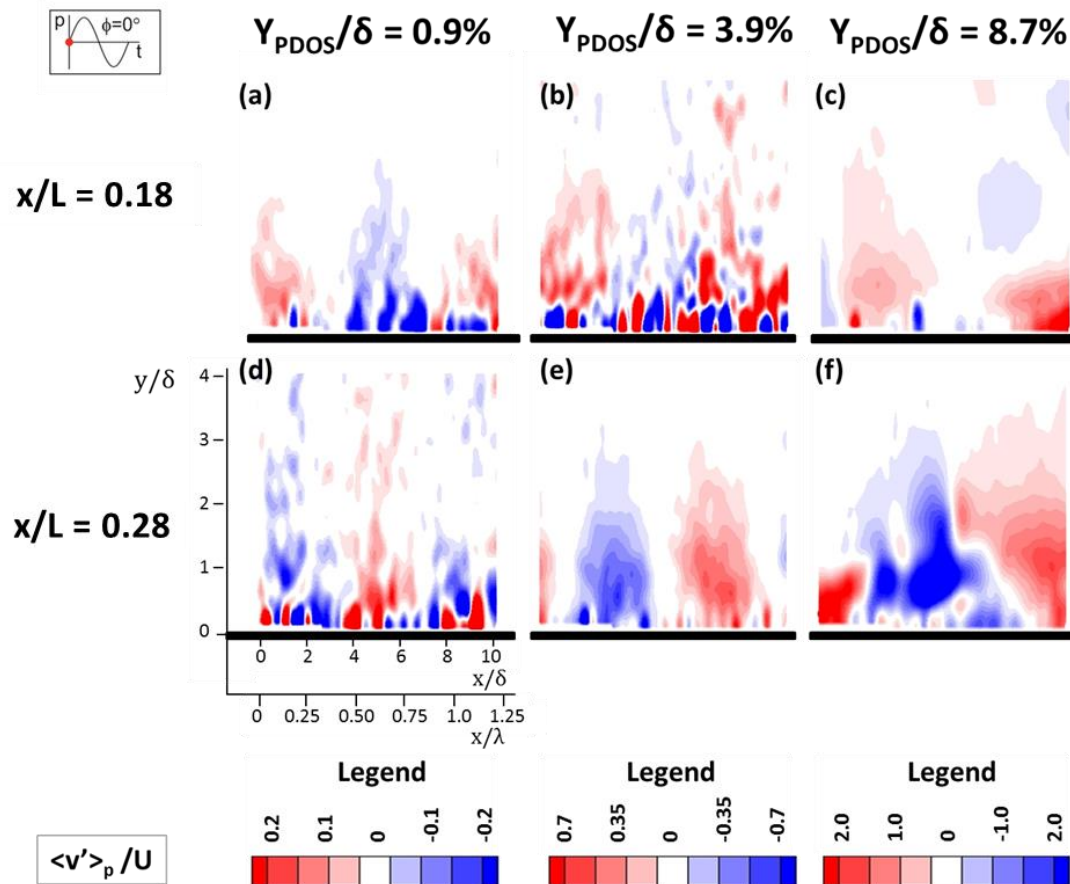


Figure 15. Phase-averaged wall-normal velocity fluctuations observed at $x/L = 0.18$ and with upstream PDOS activated at $y_{PDOS}/\delta =$ (a) 0.9%, (b) 3.9%, and (c) 8.7%, and wall-normal velocity fluctuations observed at $x/L = 0.28$ with $y_{PDOS}/\delta =$ (d) 0.9%, (e) 3.9%, and (f) 8.7%.

Based on the results of Figure 14 and 15, it was determined that an actuation level of $y_{PDOS}/\delta = 3.9\%$, provided the most coherent structures at both streamwise locations and, consequently, was the preferred level option for actuating the T-S waves. As an additional form of analysis, time-averaged velocity profiles from the center of each streamwise measurement domain (obtained using PIV) with and without actuation were compared to the Blasius solution. The results are shown in Figure 16, where the vertical axis is wall-normal distance normalized by boundary layer thickness δ for the baseline case at each location.

The velocity profiles indicate that all time-averaged PDOS actuator-driven cases at the $x/L = 0.18$ location (Figure 16a) are in excellent agreement with the Blasius solution and the baseline case (PDOS present but not actuated, shown in dark blue), suggesting that these actuation levels do not alter the mean flow. Downstream of the second PDOS actuator at $x/L = 0.28$ (Figure 16b), the two lower actuation cases, $y_{PDOS}/\delta = 0.9\%$ and 3.9% (shown in green and red, respectively), still agree well with the Blasius solution and the baseline case, indicating that these actuation levels still do not alter the mean flow field. However, when the actuation level is increased to $y_{PDOS}/\delta = 8.7\%$ (Figure 16b, in light blue) the velocity profile deviates significantly from the laminar profile. This suggests that the actuation level is large enough to affect the mean flow, which is indicative of a non-linear mechanism.

Based on the aforementioned results, the upstream PDOS was activated with a sinusoidal waveform having a frequency of 250 Hz and an actuation level of $y_{PDOS}/\delta = 3.9\%$, to excite and phase-lock the T-S waves without introducing a non-linear mechanism. In order to explore the feasibility of using the downstream PDOS to mitigate and/or enhance the T-S wave, it was actuated at the same frequency but at an actuation level of $y_{PDOS}/\delta = 8.7\%$. The increase in actuation level allows the T-S coherent structures phase-locked by the first actuator (which have grown as they advected downstream) to be roughly the same magnitude as the coherent structures phase-locked by the second actuator (which have had only very limited streamwise distance in which to grow). By matching the intensity of T-S wave phase-locked by each actuator, it becomes possible to mitigate the T-S wave using the superposition principle, which was discussed in detail in the Introduction.

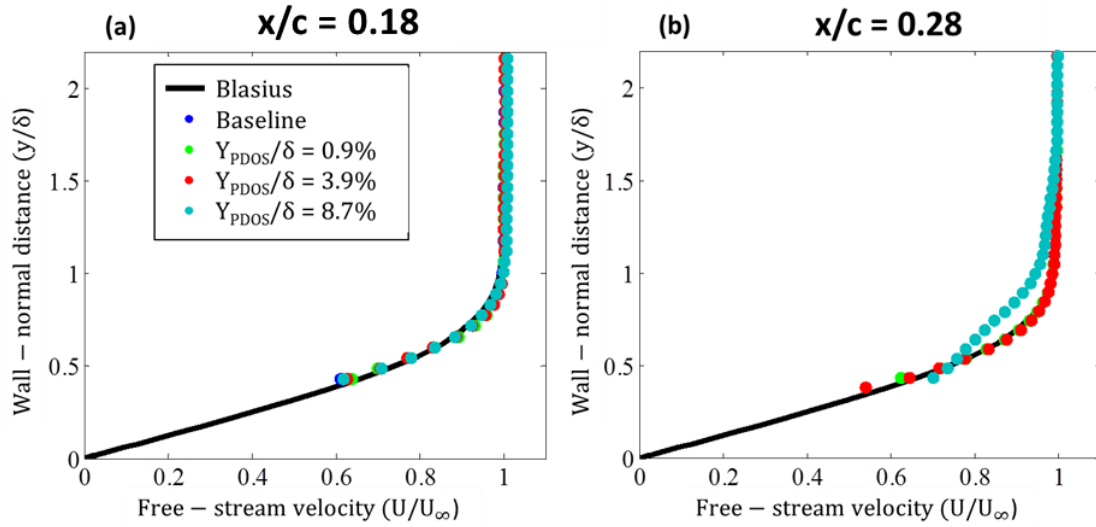


Figure 16. Time-averaged velocity profiles of the baseline case, and three excitation cases of $y_{PDOS}/\delta = 0.9\%$, 3.9% , and 8.7% at (a) $x/L = 0.18$ and (b) 0.28 . The solid line represents the Blasius solution.

Next, the effect of the phase shift between the downstream and upstream PDOS actuators was explored at phase $\phi = 0^\circ$ of the oscillation cycle. Figures 17 and 18 present the coherent streamwise, $\langle u' \rangle_p / U$, and wall-normal, $\langle v' \rangle_p / U$, velocities components, respectively. For each figure, five cases are shown: the excitation case, i.e., only upstream PDOS is activated (Figure 17e and Figure 18e, center), and four excitation-control cases (both PDOS actuators activated) at phase shifts of $\Delta\Phi = 0^\circ, 90^\circ, 180^\circ$, and 270° (Figure 17a-d and Figure 18a-d). At phase shifts of $\Delta\Phi = 90^\circ$ and 270° , shown in (Figure 17b and d, and Figure 18b and d) neither velocity component shows a significant change in the magnitude of the coherent fluctuations when compared to the excitation only (Figure 17e and Figure 18e). However, when the phase shift is $\Delta\Phi = 0^\circ$ (Figure 17a and Figure 18a), the excitation-control shows significant increase in the velocity magnitudes in comparison to the excitation case, demonstrating that the PDOS actuator can be used to enhance T-S waves in situations where hastening the transition to turbulence it desirable. In contrast, a phase shift of $\Delta\Phi = 180^\circ$ (Figure 17c and Figure 18c), decreased the magnitudes of the coherent structures, thereby demonstrating the feasibility of applying the superposition principle via the PDOS actuators to delay the transition. Note that the selections of $y_{PDOS}/\delta = 8.7\%$ and $\Delta\Phi = 180^\circ$ phase shift for the

downstream PDOS actuator were based on the growth rate of the T-S wave and its phase velocity, respectively. It should be noted that the goal of this work is to demonstrate the feasibility of the new PDOS actuator. Therefore, the phase shift of $\Delta\Phi = 180^\circ$ was not optimized, and adjustments to this parameter may reduce the coherent structures further.

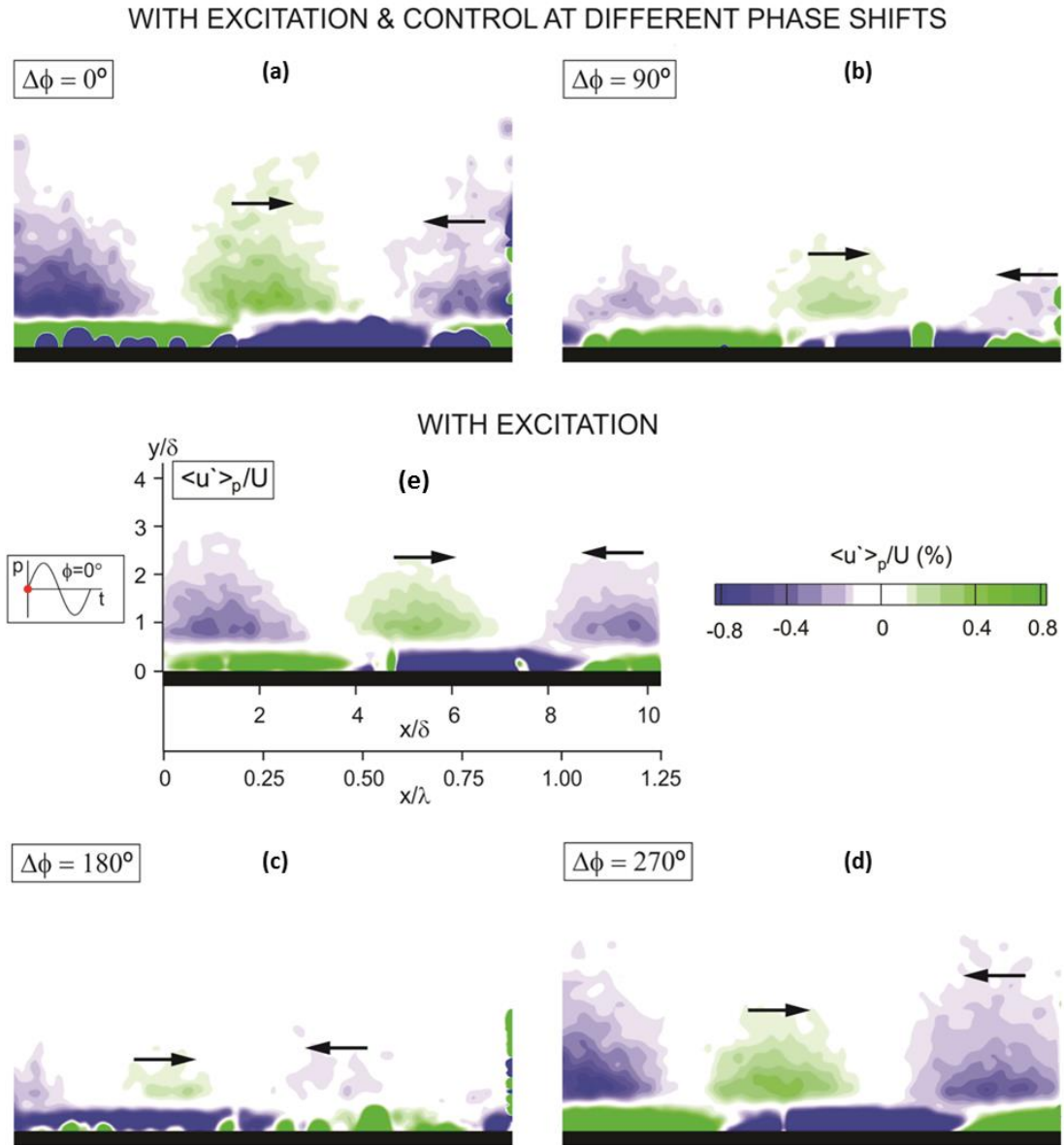


Figure 17. Phase-averaged streamwise velocity fluctuation $x/L = 0.28$ with four excitation-control cases (i.e., both PDOS actuators activated) at phase shifts (a) $\Delta\Phi = 0^\circ$, (b) $\Delta\Phi = 90^\circ$, (c) $\Delta\Phi = 180^\circ$, (d) $\Delta\Phi = 270^\circ$, and (e) with only the upstream PDOS activated (excitation).

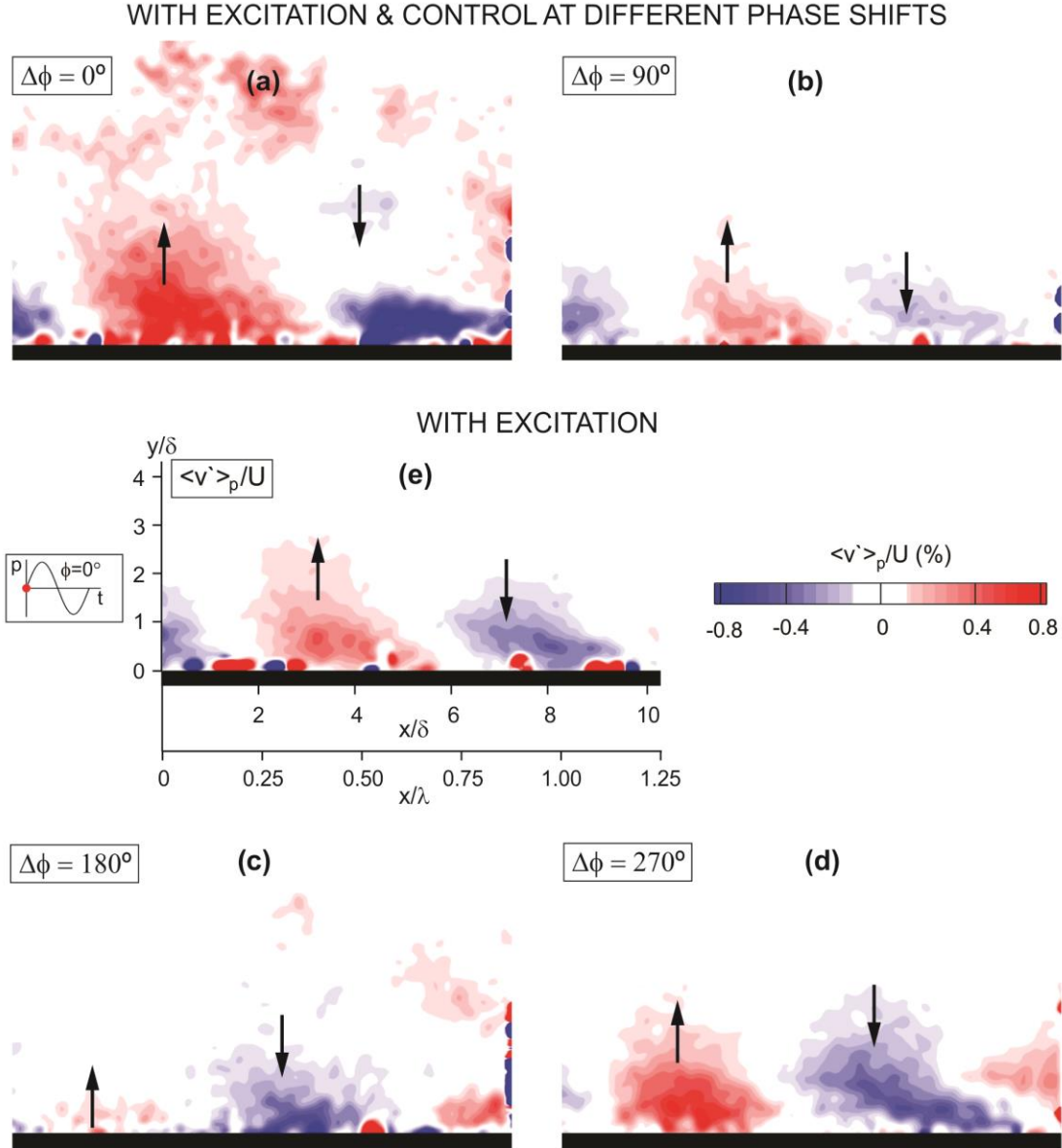


Figure 18. Phase-averaged wall-normal velocity fluctuation at $x/L = 0.28$ with four excitation-control cases (i.e., both PDOS actuators activated) at phase shifts (a) $\Delta\phi = 0^\circ$, (b) $\Delta\phi = 90^\circ$, (c) $\Delta\phi = 180^\circ$, (d) $\Delta\phi = 270^\circ$, and (e) with only the upstream PDOS activated (excitation).

Figure 19 shows color contours of the normalized phase-averaged streamwise velocity fluctuations, $\langle u' \rangle_p / U$, at the downstream interrogation window (downstream of the downstream PDOS, at $x/L = 0.28$). Blue contours indicate upstream-oriented flow, i.e., flow towards the leading edge of the flat plate, and green contours indicate downstream-oriented flow, that is, towards the trailing edge of the flat plate. Two sets of phase-averaged data are presented: (i) the excitation case (only upstream PDOS

actuated, left column), and (ii) excitation-control case (both PDOS actuators are activated, right column), for three different phases ($\phi = 0^\circ$, 120° , and 240° , Figures 19a and b, 19c and d, and 19e and f, respectively) during the excitation cycle. Activating the upstream PDOS actuator phase-locked the T-S wave, as shown in the left column. Concentrations of upstream-oriented (blue) flow and downstream-oriented (green) flow are present and appear as coherent structures which advect downstream during the actuation cycle. When both PDOS actuators are active, in order to employ excitation-control (right column), the magnitudes of these concentrations are reduced, suggesting that the combined excitation-control strategy is successful in reducing the magnitude of the T-S wave. Note that these concentrations move downstream throughout the cycle, as indicated by the dashed line. Moreover, even though the magnitude of the T-S wave structures is decreased in presence of control (i.e., when both PDOS actuators are active), the coherence of the structures is still detectable. Using the streamwise propagation of the structures, i.e., between two phases, the phase velocity of the wave was calculated to be $U_{TS} \approx 0.35U$, which compares well to the velocity calculated from stability analysis, as well as to the previous work by Duchmann et al. [58].

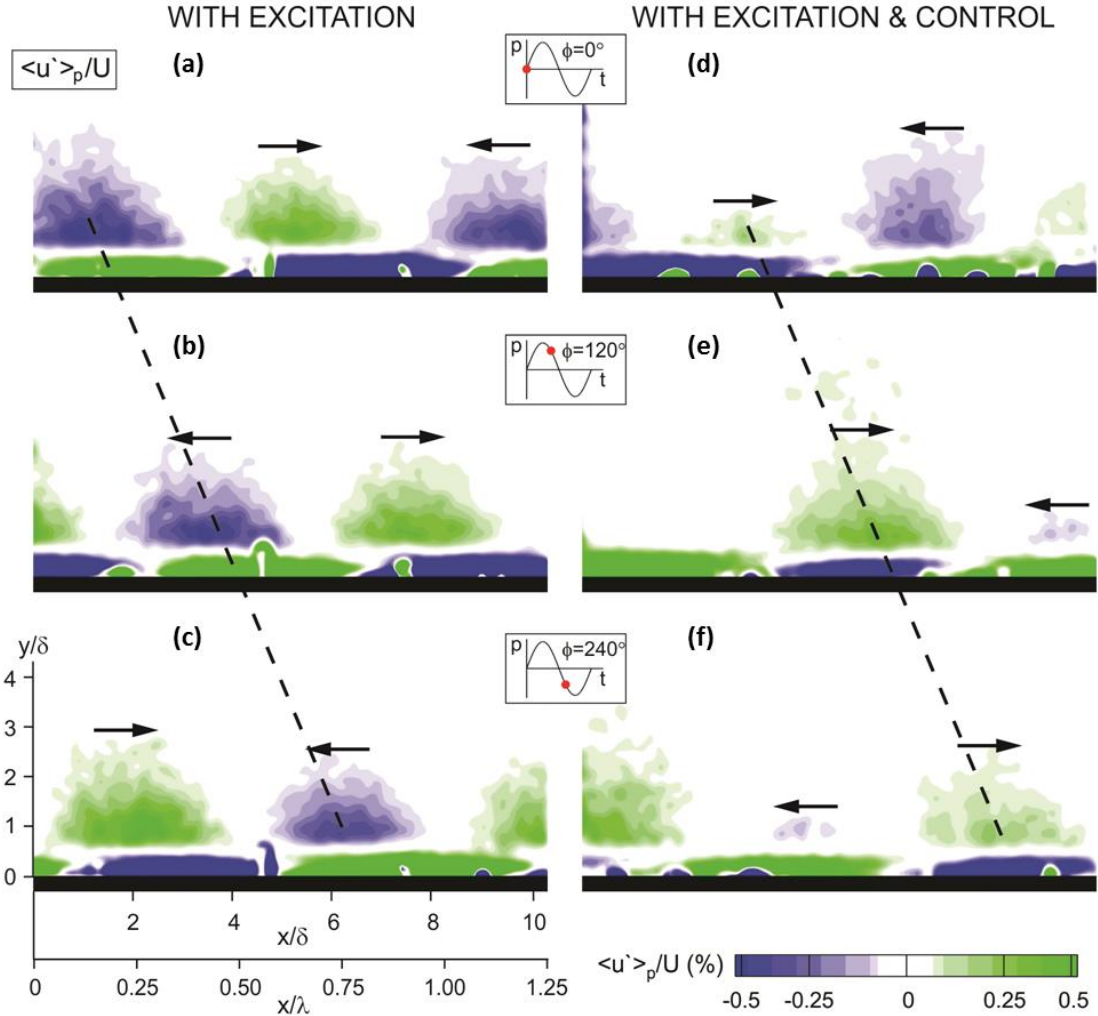


Figure 19. Phase-averaged streamwise velocity fluctuation at $x/L = 0.28$ for three phases along the excitation cycle with the upstream PDOS only (a-c) and both PDOS actuators active (d-f).

Similar results were obtained for the phase-averaged wall-normal velocity fluctuations, $\langle v' \rangle_p / U$, which are presented in Figure 20. As in previous figures, red contours indicate positive wall-normal velocity (i.e., flow away from the surface) and blue contours indicate negative wall-normal velocity (i.e., flow toward the wall). As in the previous figure, two sets of phase-averaged data are presented: (i) the excitation case (only upstream PDOS actuated, left column), and (ii) excitation-control case (both PDOS actuators are activated, right column), for three different phases ($\phi = 0^\circ$, 120° , and 240° , Figure 19a and b, 19c and d, and 19e and f, respectively) during the excitation cycle. The magnitudes and physical sizes of the wall-normal velocity fluctuations, indicated by the red and blue clusters, are larger when only the upstream PDOS actuator

is activated (left column) compared to the case where both actuators are active (right column) at the appropriate magnitudes and phase-shift for cancellation. As expected, the location of maximum positive wall-normal velocity is offset from the positive streamwise velocity component by one-half of the wavelength.

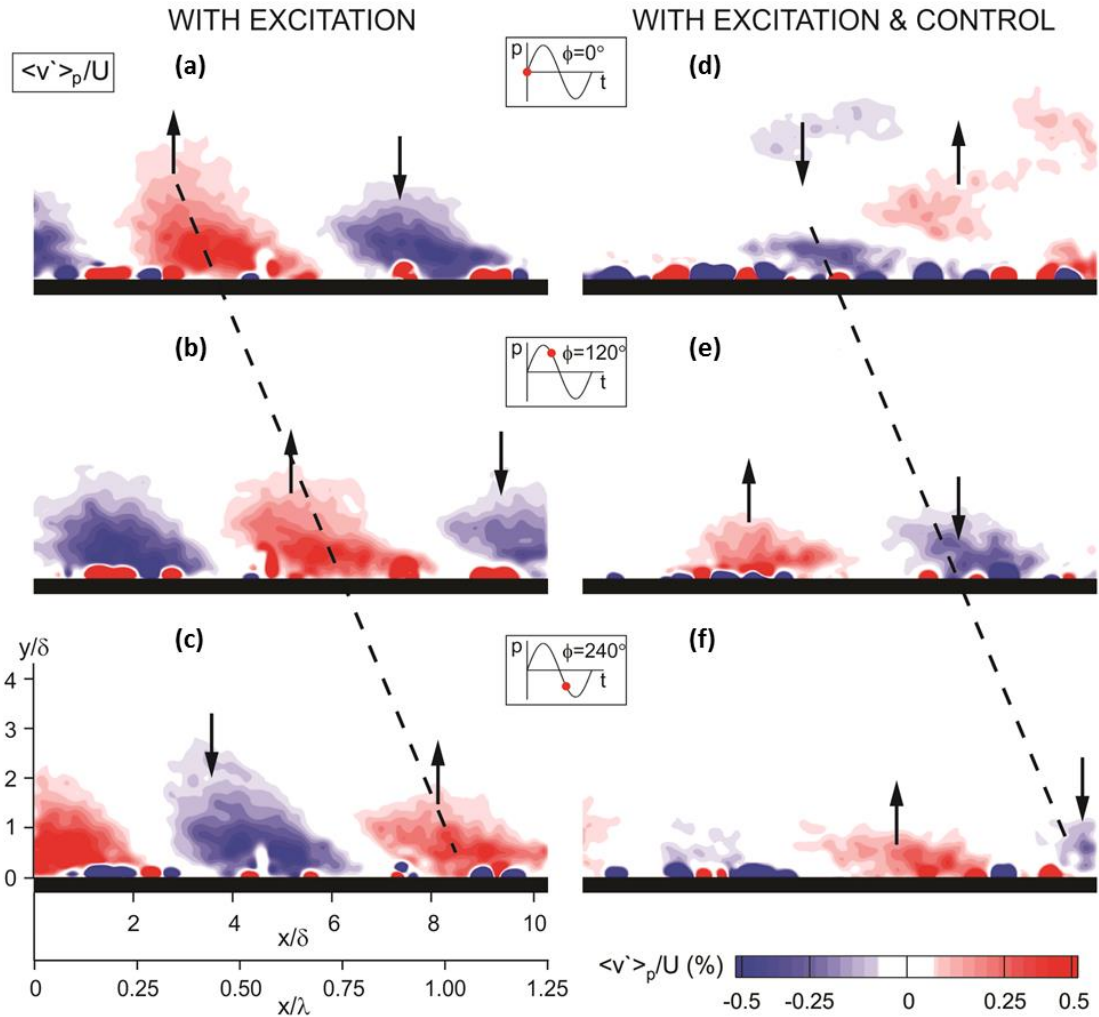


Figure 20. Phase-averaged wall-normal velocity fluctuation at $x/L = 0.28$ for three phases along the excitation cycle with the upstream PDOS only (a-c) and both PDOS actuators active (d-f).

Another way to explore the effect of the wave cancellation technique is using in-plane velocity vectors of the coherent fluctuations, as presented in Figure 21a and b, at a phase $\phi = 240^\circ$ of the actuation cycle for the excitation and excitation-control cases, respectively. Since the time-averaged velocity field was subtracted from the phase-

averaged fields, the vector arrows indicate flow direction and relative magnitude of the downstream propagating coherent structures. This provides a quantitative way to visualize the coherent structures within the flow. As can be seen, the magnitude of the velocity vectors is significantly reduced through the use of the wave cancellation technique.

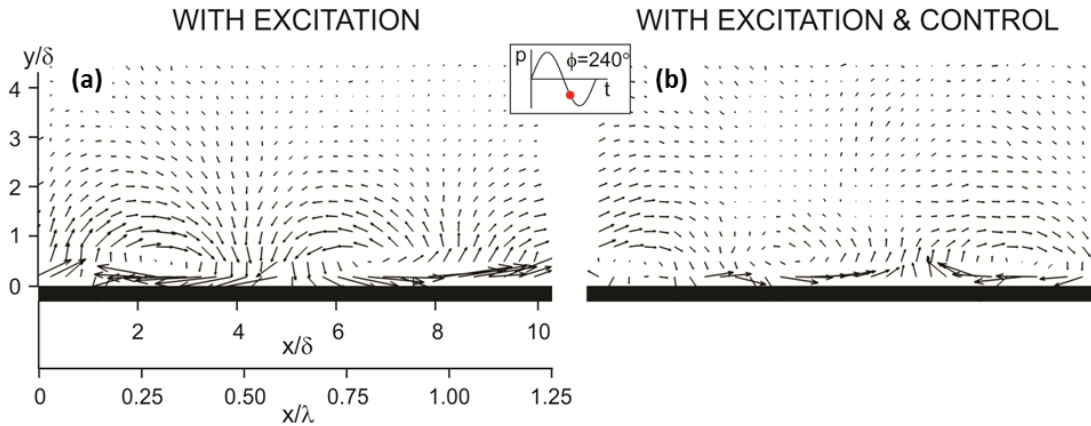


Figure 21. Phase-averaged velocity vector fields at $\phi = 240^\circ$ with (a) excitation only and (b) excitation-control.

Finally, the reduction of the coherent streamwise and wall-normal velocity magnitudes was also quantified using boundary layer profiles, as shown in Figure 22a and b, respectively. Each plot includes four sets of data, corresponding to the phase-averaged velocity fluctuation at the streamwise location of maximum and minimum amplitudes of the phase-locked structures. As can be seen, the magnitude of the negative streamwise fluctuation was reduced from $\langle u' \rangle_p / U = 1.5$ to 0.4, corresponding to 73% reduction in the total magnitude of the coherent structures compared to the excitation case. Moreover, the positive peak was reduced from $\langle u' \rangle_p / U = 2.5$ to 0.8, which is a reduction of 68% in magnitude. A similar change in the highest magnitudes of positive and negative values of the wall-normal is seen in Figure 22b where a reduction in the coherent velocity fluctuations of 67% was achieved. These reductions in magnitude demonstrate the feasibility of using discrete surface roughness elements in the form of PDOS to suppress T-S waves.

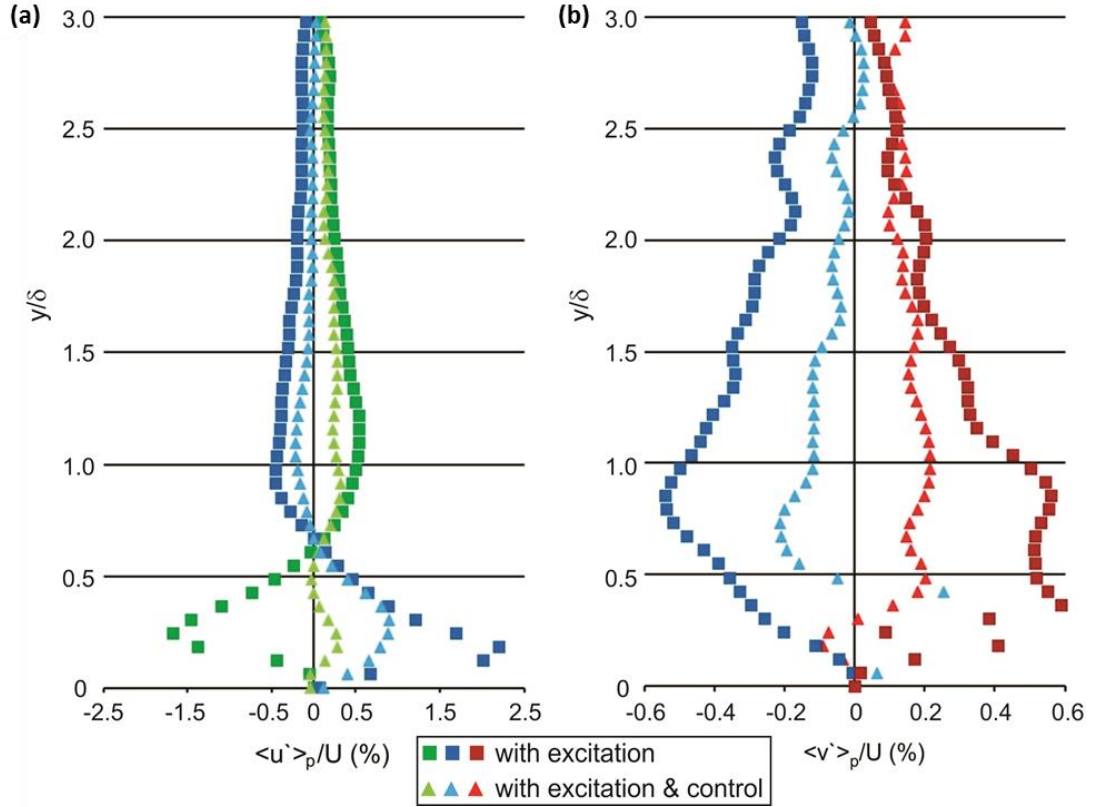


Figure 22. Wall-normal distributions of the velocity fluctuations for maximum amplitude phase-locked structures of the (a) streamwise component and (b) wall-normal component.

Stability analysis was conducted using the Orr-Sommerfeld equation (as cited by Schlichting & Gersten,[1]) which was solved in order to determine the most amplified frequency for the Tollmien-Schlichting wave:

$$(U - c)(\varphi'' - \alpha^2 \varphi) - U'' \varphi = -\frac{i}{\alpha Re} (\varphi'''' - 2\alpha^2 \varphi'' + \alpha^4 \varphi) \quad (2)$$

Flow instabilities were considered to be linear, based on velocity profile results. The Orr-Sommerfeld equation was solved to determine the most amplified frequency. In addition, data obtained at streamwise locations $x/L = 0.18$ and 0.28 were considered, where the Reynolds numbers based on the displacement thickness were $Re_{\delta^*} = 1,084$ and $1,531$ respectively. From these values the streamwise wavelength, λ , and the frequency, ω^* , of the most amplified T-S wave were calculated using:

$$\lambda = \frac{\omega U}{2\pi \delta^*} \quad (3)$$

where α_r is the wave number. Based on the equations 3 and 4, the calculated values for the most amplified T-S wave wavelength were $\lambda = 24\text{mm}$ and $\omega^* = 250$ Hz. Based on these results and the stability calculations of Kotsonis et al., the stability locations of the two PDOS actuators were plotted, where the non-dimensional frequency F was defined as:

$$F = \frac{\omega}{Re_{\delta^*}} \quad (4)$$

where ω is the local non-dimensional frequency of the most amplified mode, given by:

$$\omega = \frac{2\pi\delta^*f}{Re_{\delta^*}} \quad (5)$$

Figure 23 (after Kotsonis et al., [44]) shows the results of stability calculations. Non-dimensional frequency, F is shown on the vertical axis and Reynolds number based on boundary layer thickness, Re_{δ} , is shown on the horizontal axis. The neutral stability curve is shown in black. The locations of the upstream and downstream PDOS actuators are superimposed in red; note that the actual frequency used in this work was $f = 250$ Hz. Based on these values (and the stability map of Kotsonis et al., [44]), it was found that the location of the upstream PDOS actuator is in the unstable region (i.e., instabilities in the flow will be amplified), whereas the downstream PDOS actuator is in the stable region. Therefore, once T-S waves have been suppressed, the flow is anticipated to remain laminar farther downstream. Resultantly, it is believed that no additional rows of actuators will be necessary to maintain laminar flow. However, future work is necessary to evaluate the veracity of this assertion.

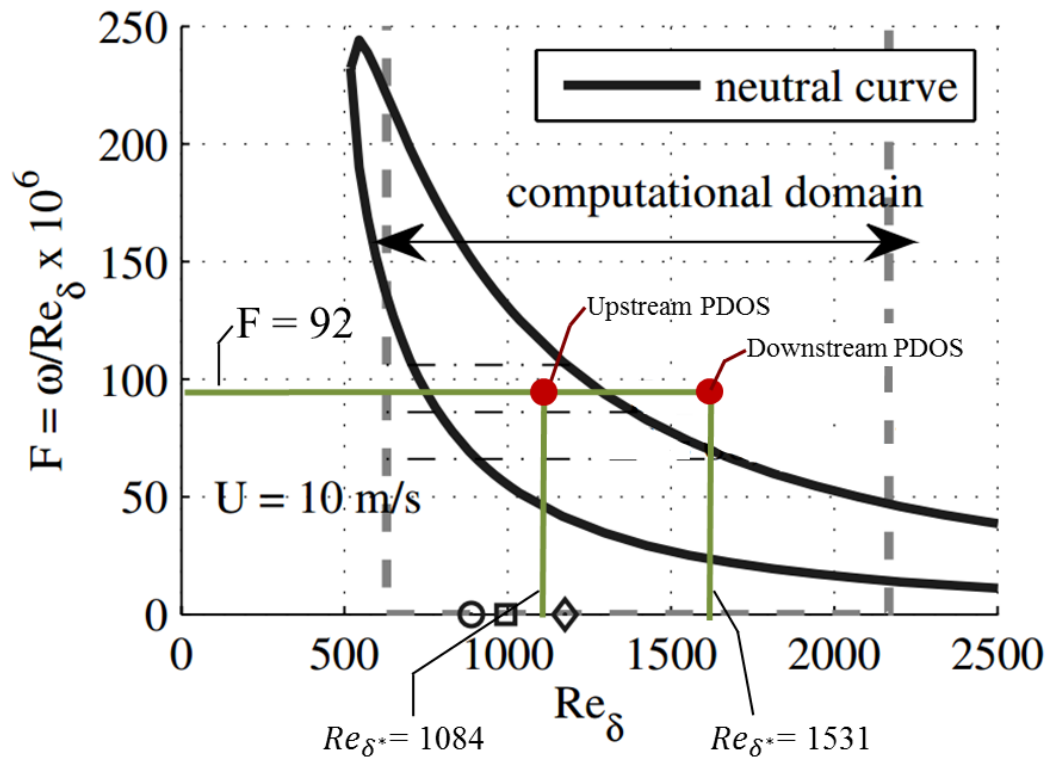


Figure 23. Neutral stability curve (after Kotsonis et al., [44]) with locations of the upstream and downstream PDOS actuators superimposed in red.

5. CONCLUSIONS

A feasibility study to delay the transition from laminar to turbulent flow over a flat plate, using the wave cancellation technique via dynamic surface modification, was conducted. A traditional form of oscillating surface, the Electro Active Polymer (EAP) actuator, was tested and found to be insufficient for this application. To address this, a new actuator, the Piezoelectrically-Driven Oscillating Surface (PDOS) was designed and built. First, the PDOS actuator was quantified using a laser displacement sensor for a range of actuation frequencies and design parameters. Circular and elliptical slot dimples were tested, as well as several thicknesses of rubber and neck heights. The final configuration utilized a 0.79 mm thick ultra-strength neoprene rubber surface with a 12.7 mm diameter circular dimple, a cavity height of 2 mm, and a neck height of 2 mm.

For the selected actuator geometry, it was found that the PDOS actuator's peak-to-peak deflection increased linearly as a function of the input voltage with a slope that depended on driving frequency. For the present work, an actuation frequency of 250 Hz was selected, based on linear stability analysis, using the experimental velocity profile, and previous work by Widmann et al. [39], [41].

Two PDOS actuators were mounted flush with the surface of the flat plate, separated by a streamwise distance of $x/L = 0.1$. Driving voltages of 25 V, 100 V, and 200 V (with a corresponding normalized peak-to-peak displacement of $y_{PDOS}/\delta = 0.9\%$, 3.9% , and 8.7% , respectively) were applied to the first actuator and the effect of PDOS actuation on coherent fluctuations was observed at two streamwise locations using PIV. For the lowest actuation level, $y_{PDOS}/\delta = 0.9\%$, the T-S waves were successfully phase-locked, but their magnitude was small and they did not appear coherent ($\langle u' \rangle / U \approx 0.25\%$). By increasing the actuation level to $y_{PDOS}/\delta = 3.9\%$, the magnitude of the streamwise and wall-normal velocity fluctuations was approximately doubled. Moreover, coherent structures were well-defined ($\langle u' \rangle / U \approx 0.5\%$). At the highest actuation level used in the present work, $y_{PDOS}/\delta = 8.7\%$, the magnitude of the coherent fluctuations increased by a factor of 10, and at $x/L = 0.28$ the mean flow was significantly affected by the actuation, suggesting that non-linear effects dominate the transition process. In all cases, coherent structures were observed with a phase velocity of $0.35U$, similar to the value predicted from stability analysis.

Once the feasibility of using the PDOS actuator to phase-lock T-S waves was established, a second downstream actuator was activated (in conjunction with the upstream actuator) at the proper amplitude and phase shift to mitigate the artificially excited structures. It was shown that when the upstream actuator was driven at $y_{PDOS}/\delta = 3.9\%$ and the downstream actuator was activated at $y_{PDOS}/\delta = 8.7\%$ and with a phase shift of $\Delta\Phi = 180^\circ$ (with respect to the upstream actuator) the magnitude of the coherent fluctuations were successfully and significantly reduced. This work demonstrated the feasibility of using the PDOS actuators to either enhance or suppress T-S waves and thus to promote or delay, respectively, the transition to turbulence. Note that the phase shift between the two PDOS actuators, as well as the relative driving voltages, was not optimized to provide the most effective control. Nevertheless, this study successfully demonstrated the feasibility of using discrete oscillating surfaces, in the form of PDOS actuators, as a means of active control for boundary layer transition.

RECOMMENDATIONS FOR FUTURE WORK

This work successfully used a flat plate with discrete dynamic surface roughness (i.e., the PDOS actuator) to phase-lock the Tollmien-Schlichting wave at the most amplified frequency (250 Hz) and observe it using Particle Image Velocimetry. The feasibility of controlling the T-S wave was demonstrated by engaging a second, downstream PDOS actuator at an appropriate phase and amplitude in order to mitigate the coherent structures. The success and methodology of this work should be used to guide future work and significant work is possible:

1. Conduct PIV experiments to confirm the hypothesis that the T-S wave will not continue to grow downstream of the second actuator
2. Use SPIV to obtain volumetric measurements of flow field behavior beyond the flat plate's centerline
3. Apply these techniques to engage in T-S wave observation and control on airfoil models, wherein the presence of an adverse pressure gradient may provide an additional challenge

4. Develop two arrays of PDOS actuators to phase-lock and control the T-S wave across the span of the model
5. Investigate close-loop control methodologies to automatically phase-lock and control the T-S wave based on flow conditions

REFERENCES

- [1] H. Schlichting and K. Gersten, *Boundary-Layer Theory*, 8th ed. New York: Springer-Verlag, 2001.
- [2] Y. S. Kachanov, “Physical Mechanisms of Laminar-Boundary-Layer Transition,” *Annu. Rev. Fluid Mech.*, vol. 26, no. 1, pp. 411–482, 1994.
- [3] A. Michalke, “On the inviscid instability of the hyperbolictangent velocity profile,” *J. Fluid Mech.*, vol. 19, no. 4, pp. 543–556, 1964.
- [4] H. Opfer, “Active cancellation of 3D Tollmien-Schlichting waves in the presence of sound and vibrations,” PhD Dissertation, Mathematics and Natural Sciences, University of Göttingen, Göttingen, Germany, 2002.
- [5] M. Gaster, “A note on the relation between temporally-increasing and spatially-increasing disturbances in hydrodynamic stability,” *J. Fluid Mech.*, vol. 14, no. 2, pp. 222, 1962.
- [6] M. Gaster, “On the generation of spatially growing waves in a boundary layer,” *J. Fluid Mech.*, vol. 22, no. 3, pp. 433, 1965.
- [7] R. Jordinson, “The flat plate boundary layer. Part 1. Numerical integration of the Orr-Sommerfeld equation,” *J. Fluid Mech.*, vol. 43, no. 4, pp. 801, 1970.
- [8] G. B. Schubauer and H. K. Skramstad, “Laminar boundary layer oscillations and transition on a flat plate,” *NACA Tech. Rep. 909 (1948) Originally issued as NACA ACR*, vol. 2386. pp. 161, 1985.
- [9] A. V. Boiko, K. J. A. Westin, B. G. B. Klingmann, V. V. Kozlov, and P. H. Alfredsson, “Experiments in a boundary layer subjected to free stream turbulence. Part 2. The role of TS-waves in the transition process,” *J. Fluid Mech.*, vol. 281, no. 1, pp. 219, 1994.
- [10] W. S. Saric, H. L. Reed, and E. J. Kerschen, “Boundary-Layer Receptivity to Free-Stream Disturbances,” *Annu. Rev. Fluid Mech.*, vol. 34, no. 1, pp. 291–319, 2002.
- [11] R. W. Milling, “Tollmien–Schlichting wave cancellation,” *Phys. Fluids*, vol. 24, no. 5, pp. 979, 1981.
- [12] H. W. Liepmann, G. L. Brown, and D. M. Nosenchuck, “Control of laminar-instability waves using a new technique,” *J. Fluid Mech.*, vol. 118, pp. 187–200,

1982.

- [13] A. S. W. Thomas, "The control of boundary layer transition using a wave-superposition principle," *J. Fluid Mech.*, vol. 137, no. 1, pp. 233–249, 1983.
- [14] D. Sturzebecher and W. Nitsche, "Active cancellation of Tollmien–Schlichting instabilities on a wing using multi-channel sensor actuator systems," *Int. J. Heat Fluid Flow*, vol. 24, no. 4, pp. 572–583, 2003.
- [15] P. S. Klebanoff, K. D. Tidstrom, and L. M. Sargent, "The three-dimensional nature of boundary-layer instability," *J. Fluid Mech.*, vol. 12, no. 1, pp. 1, 1962.
- [16] M. V Morkovin, "Critical Evaluation of Transition From Laminar To Turbulent Shear Layers With Emphasis on Hypersonically Traveling Bodies," No. RIAS-TR-68-13C, Martin Marietta Corp., Baltimore, MD Research Inst. for Advanced Studies, 1969.
- [17] M. V Morkovin, "Bypass-Transition Research: Issues and Philosophy," in *Instabilities and Turbulence in Engineering Flows*, 1993, pp. 3–30. Springer Netherlands. 10.1007/978-94-011-1743-2_1
- [18] J. A. Ross, F. H. Barnes, J. G. Burns, and M. A. S. Ross, "The flat plate boundary layer. Part 3. Comparison of theory with experiment," *J. Fluid Mech.*, vol. 43, no. 4, pp. 819, 1970.
- [19] M. D. J. Barry and M. A. S. Ross, "The flat plate boundary layer. Part 2. The effect of increasing thickness on stability," *J. Fluid Mech.*, vol. 43, no. 4, pp. 813–818, 1970.
- [20] H. Fasel and U. Konzelmann, "Non-parallel stability of a flat-plate boundary layer using the complete Navier-Stokes equations," *J. Fluid Mech.*, vol. 221, pp. 311–347, 1990.
- [21] N. Lin, H. L. Reed, and W. S. Saric, "Effect of leading-edge geometry on boundary-layer receptivity to freestream sound," *Instab. Transition and Turbul.*, (ed. M. Hussaini, A. Kumar & C. Streett), pp. 421–440, 1992.
- [22] P. J. Shapiro, *The influence of sound upon laminar boundary layer instability*. No. A/V-83458-83560-1. Massachusetts Inst. of Tech. Cambridge Acoustics and Vibration Lab, 1977.
- [23] M. E. Goldstein, "Scattering of acoustic waves into Tollmien-Schlichting waves

- by small streamwise variations in surface geometry,” *J. Fluid Mech.*, vol. 154, pp. 509–529, 1985.
- [24] J. D. Crouch, “Distributed excitation of Tollmien-Schlichting disturbances waves by vertical free-stream disturbances,” vol. 6, no. 1, pp. 217–223, 1994.
- [25] L. E. Hunt and W. S. Saric, “Boundary-Layer Receptivity to Three-Dimensional Roughness Arrays on a Swept-Wing,” *41st AIAA Fluid Dynamics Conference and Exhibit.*, Honolulu, HI, 2011, pp. 1–25.
- [26] M. Gad-el-Hak, *Flow Control: Passive, Active, and Reactive Flow Management*, Cambridge University Press, 2000.
- [27] J. H. M. Fransson, A. Talamelli, L. Brandt, and C. Cossu, “Delaying Transition to Turbulence by a Passive Mechanism,” *Phys. Rev. Lett.*, vol. 96, no. 6, pp. 064501, 2006.
- [28] J. C. Lin, “Review of research on low-profile vortex generators to control boundary-layer separation,” *Progress in Aerospace Science*, vol. 38, no. 4, pp. 389–420, 2002.
- [29] K. B. M. Q. Zaman, D. J. McKinzie, and C. L. Rumsey, “A natural low-frequency oscillation of the flow over an airfoil near stalling conditions,” *J. Fluid Mech.*, vol. 202, pp. 403–442, 1989.
- [30] G. Godard and M. Stanislas, “Control of a decelerating boundary layer. Part 1: Optimization of passive vortex generators,” *Aerosp. Sci. Technol.*, vol. 10, no. 3, pp. 181–191, 2006.
- [31] L. N. Cattafesta and M. Sheplak, “Actuators for Active Flow Control,” *Annu. Rev. Fluid Mech.*, vol. 43, pp. 247–272, 2011.
- [32] O. H. Wehrmann, “Tollmien-Schlichting Waves under the Influence of a Flexible Wall,” *Phys. Fluids*, vol. 8, no. 7, pp. 1389, 1965.
- [33] R. D. Joslin, R. A. Nicolaidis, G. Erlebacher, M. Y. Hussaini, and M. D. Gunzburger, “Active control of boundary-layer instabilities: Use of sensors and spectral controller,” *AIAA J.*, vol. 33, no. 8, pp. 1521–1523, 1995.
- [34] R. D. Joslin, G. Erlebacher, and M. Y. Hussaini, “Active control of instabilities in laminar boundary layers—Overview and concept validation,” *J. Fluids Eng.*, vol. 118, no. 3, pp. 494, 1996.

- [35] H. W. Liepmann and D. M. Nosenchuck, "Active control of laminar-turbulent transition," *J. Fluid Mech.*, vol. 118, pp. 201–204, 1982.
- [36] N. R. Losse, R. King, M. Zengl, U. Rist, and B. R. Noack, "Control of Tollmien–Schlichting instabilities by finite distributed wall actuation," *Theor. Comput. Fluid Dyn.*, vol. 25, no. 1–4, pp. 167–178, 2011.
- [37] C. L. Enloe *et al.*, "Mechanisms and Responses of a Dielectric Barrier Plasma Actuator: Geometric Effects," *AIAA J.*, vol. 42, no. 3, pp. 595–604, 2004.
- [38] T. C. Corke, C. L. Enloe, and S. P. Wilkinson, "Dielectric Barrier Discharge Plasma Actuators for Flow Control," *Annu. Rev. Fluid Mech.*, vol. 42, no. 1, pp. 505–529, 2010.
- [39] A. Widmann, A. Duchmann, A. Kurz, S. Grundmann, and C. Tropea, "Measuring Tollmien–Schlichting waves using phase-averaged particle image velocimetry," *Exp. Fluids*, vol. 53, no. 3, pp. 707–715, 2012.
- [40] A. Duchmann, A. Kurz, A. Widmann, S. Grundmann, and C. Tropea, "Characterization of Tollmien-Schlichting Wave Damping by DBD Plasma Actuators Using Phase-Locked PIV," *50th AIAA Aerospace Sciences Meeting Including the New Horizons Forum Aerospace Exposition.*, Nashville, TN., pp. 1-9.
- [41] A. Widmann, A. Kurz, B. Simon, S. Grundmann, and C. Tropea, "Characterization of the Interaction between Tollmien-Schlichting Waves and a DBD Plasma Actuator using Phase-locked PIV," *10th International Symposium on Particle Image Velocimetry*, Delft, The Netherlands., 2013, pp. 1-9.
- [42] S. Grundmann and C. Tropea, "Experimental damping of boundary-layer oscillations using DBD plasma actuators," *Int. J. Heat Fluid Flow*, vol. 30, no. 3, pp. 394–402, 2009.
- [43] S. Grundmann and C. Tropea, "Active cancellation of artificially introduced Tollmien–Schlichting waves using plasma actuators," *Exp. Fluids*, vol. 44, no. 5, pp. 795–806, 2008.
- [44] M. Kotsonis, R. Giepmans, S. Hulshoff, and L. Veldhuis, "Numerical Study of the Control of Tollmien–Schlichting Waves Using Plasma Actuators," *AIAA J.*, vol. 51, no. 10, pp. 2353–2364, 2013.

- [45] M. Engert and P. Andreas, "Active Cancellation of Tollmien-Schlichting Instabilities in Compressible Flows Using Closed-Loop Control," in *IUTAM Symposium on Flow Control and MEMS*, London, England, 2008, pp. 319–331.
- [46] A. Kurz, C. Tropea, S. Grundmann, S. Interfaces, and T. U. Darmstadt, "Development of Active Wave Cancellation using DBD Plasma Actuators for In-flight Transition Control," 6th AIAA Flow Control Conference, Nummer AIAA, vol. 2946, pp. 1–6, 2012.
- [47] K. Barckmann, C. Tropea, and S. Grundmann, "Attenuation of Tollmien–Schlichting Waves Using Plasma Actuator Vortex Generators," *AIAA J.*, vol. 53, no. 5, pp. 1384–1388, 2015.
- [48] R. de Quadros, S. Grundmann, C. Tropea, J. Elsemueller, and S. Ulbrich, "Numerical Optimization of DBD Plasma Actuator Operating Parameters for Active Wave Cancellation Using Sinusoidal Modulation," in *6th International Symposium on Turbulence and Shear Flow Phenomena*, Seoul, Korea, pp. 766–770, 2009.
- [49] S. S. Dearing, S. Lambert, and J. Morrison, "Flow control with active dimples," *Aeronaut. J.*, vol. 111, no. 1125, pp. 705–714, 2007.
- [50] T. Van Buren and M. Amitay, "Control of a Transitioning Boundary Layer using Surface-Mounted Electro Active Polymers," *Int. J. Flow Control*, vol. 4, no. 3+4, pp. 133–145, 2012.
- [51] E. P. DeMauro, H. Dell’Orso, S. Zaremski, C. M. Leong, and M. Amitay, "Control of Laminar Separation Bubble on NACA 0009 Airfoil Using Electroactive Polymers," *AIAA J.*, vol. 53, no. 8, pp. 2270–2279, 2015.
- [52] U. Rist and K. Augustin, "Control of Laminar Separation Bubbles Using Instability Waves," *AIAA J.*, vol. 44, no. 10, pp. 2217–2223, 2006.
- [53] J. L. Pinkerton and R. W. Moses, "A Feasibility Study to Control Airfoil Shape Using Thunder," *NASA Technical Memorandum 4767*. 1997.
- [54] E. J. Abdullah, C. Bil, and S. Watkins, "Application of Smart Materials for Adaptive Airfoil Control," 47th AIAA Arospace Sciences Meeting Including the New Horizons Forum and Aerospace Exposition, Orlando, FL., pp. 1–11, 2009.
- [55] N. Udovitchik and J. Morrison, "Investigation of Active Dimple Actuators for

- Separation Control,” in *3rd AIAA Flow Control Conference*, 2006, no. June, pp. 1–9.
- [56] M. Amitay, B. A. Tuna, and H. Dell’Orso, “Identification and Mitigation of T-S Waves using Localized Dynamic Surface Modification,” *Phys. Fluids*, vol. 28, no. 6, pp. 064103, 2016.
- [57] H. Dell’Orso *et al.*, “Control of Tollmien-Schlichting Waves Using Piezoelectrically Driven Oscillating Surface,” in *AIAA Aviation 45th Annual Fluid Dynamics Conference*, Dallas, TX, 2015.
- [58] A. Duchmann, A. Reeh, R. Quadros, J. Kriegseis, and C. Tropea, “Linear Stability Analysis for Manipulated Boundary-Layer Flows using Plasma Actuators,” in *Seventh IUTAM Symposium on Laminar-Turbulent Transition*, Stockholm, Sweden, pp. 153–158, 2010.